Copper(II) complexes with 1,5-bis(2-hydroxybenzaldehyde) carbohydrazone

Diana Dragancea[a], Sergiu Shova[b], Éva A. Enyedy[c], Martin Breza[d], Peter Rapta[d], Luca M. Carrella[e], Eva Rentschler[e], Anatolie Dobrov[f], Vladimir B. Arion[f,*]

[a] *Institute of Chemistry of the Academy of Sciences of Republic of Moldova, Academiei Str. 3, MD-2028 Chisinau, Moldova*

[b] *"Petru Poni" Institute of Macromolecular Chemistry, Aleea Gr. Ghica Voda 41A, 700487 Iasi, Romania*

[c] *Department of Inorganic and Analytical Chemistry, University of Szeged, Dóm tér 7, H-6720 Szeged, Hungary*

[d] *Slovak University of Technology, Institute of Physical Chemistry and Chemical Physics, Radlinského 9, 81237 Bratislava, Slovakia*

[e] *Institute of Inorganic and Analytical Chemistry, Johannes Gutenberg University of Mainz, Duesbergweg 10-14, D-55128 Mainz, Germany*

[f] *Institute of Inorganic Chemistry of the University of Vienna, Währinger Strasse 42, A-1090 Vienna, Austria*

*corresponding author. Telephone/fax number: +43 1 427752615/+43 1 42779526; E-mail: vladimir.arion@univie.ac.at

Abstract

The acid-base properties of 1,5-bis(2-hydroxybenzaldehyde)carbohydrazone (H_4L) and its thioanalogue 1,5-bis(2-hydroxybenzaldehyde)thiocarbohydrazone (H_4L^S) have been studied experimentally by pH-potentiometry and UV−vis spectrophotometry and theoretically by using DFT methods. Copper(II) complexes $[Cu_2(HL)(DMSO)_2(H_2O)]NO_3 \cdot H_2O$ (**1**), $[\{Cu_2(HL)(DMF)(H_2O)\}_n][\{Cu_2(HL)(DMF)NO_3\}_n](NO_3)_n$ (**2**), $[Cu_2(HL)(DMF)_2(H_2O)]HSO_4 \cdot H_2O$ (**3**), $[Cu_2(HL)(DMF)_2(H_2O)]$ $[Cu_2(HL)(SO_4)(H_2O)(DMF)_2] \cdot 2H_2O$ (**4**) and $[Cu_4(HL)_2(HSO_4)(DMF)_2]HSO_4$ (**5**), where H_4L = 1,5-bis(2-hydroxybenzaldehyde)carbohydrazone, have been synthesised. Complexes **1**–**3** have been characterised by elemental analysis, IR spectroscopy, ESI mass spectrometry, cyclic voltammetry, magnetic susceptibility measurements and X-ray diffraction, while **4** and **5** only by X-ray crystallography. X-ray diffraction revealed that the ditopic triply deprotonated ligand possesses two binding sites able to accommodate transition metal ions, namely ONN and ONO. Magnetic measurements showed antiferromagnetic interactions between copper(II) centres.

Highlights

► Experimental and calculated p*K*a values for 1,5-bis(2-hydroxybenzaldehyde)carbohydrazone and 1,5-bis(2-hydroxybenzaldehyde)-thiocarbohydrazone were reported and discussed. ► Five new copper(II) complexes with 1,5-bis(2-hydroxybenzaldehyde)carbohydrazone were synthesised and characterised. ► Formation of 1D, 2D and 3D supramolecular arrays was shown by X-ray crystallography. ► There are antiferromagnetic interactions among the adjacent copper ions in complexes prepared.

Keywords: copper(II), magnetic properties, carbohydrazone, thiocarbohydrazone, Schiff base, X-ray crystallography

1. Introduction

The synthesis of high nuclearity transition metal complexes continues to attract the attention of researchers. The nuclearity of clusters is difficult to control, and synthesis of such systems requires an ingenious approach to the design of the ligands used. Polytopic ligands having well-defined and separated binding sites are suitable for synthesis of complexes with a predefined nuclearity. Ligands with hydrazone groups connected by oxalic or malonic central fragments are well-documented in the literature.[1,2,3,4] Carbohydrazide, the symmetrical derivative of hydrazine and carbonic acid, could serve as a perfect candidate for synthesis of ditopic ligands suitable for further assembly of polynuclear systems. Carbohydrazones have previously served as building blocks in the self-assembly of tetranuclear iron(II), nickel(II), cobalt(II), zinc(II) and cadmium(II) molecular squares,[5,6,7,8,9] with those of iron exhibiting interesting spin transitions.

Reactions of 1,5-bis(2-pyridylmethylene)carbohydrazide with copper(II) and nickel(II) produced dinuclear complexes.[10,11] New square self-assembled tetranuclear Ln(III) grid motifs have been prepared, using construction principles developed for first row transition metal ions.[12,13] Unusual combination of bridging $O_{hydrazone}$ groups, azides, and a central μ_4–O bridge in a $Dy(III)_4$ grid led to SMM behaviour, with significant barriers to magnetisation reversal, and two clearly discernible relaxation processes.

For carbohydrazones two tautomeric forms are possible: keto and enol.[14] The enol tautomer can adopt a *syn* or *anti* configuration because of the double-bond character of the central N-C linkage (Chart 1). The *syn* configuration is essential for getting square architectures, where the enolic oxygen is involved in the bridging of carbohydrazone ligands, with the same coordination site. The *anti* configuration was observed in dinuclear compounds, where metal ions are bridged by the N−N diazine fragment of bis-tridentate ligand. 1,5-Bis(2-hydroxybenzaldehyde)carbohydrazone (H_4L) and other closely related ligands crystallize in keto form adopting *syn* configuration as found by X-ray crystallography studies.[15,16,17,18] There are also a few reports on dioxomolybdenum(VI) and diorganotin(IV) complexes with H_4L[19,20] and on copper(II) complexes with related ligands containing *tert*-butyl groups in positions 3 and 5 of 2-hydroxybenzaldehyde moiety.[21] These reported compounds are mono- or dinuclear, while the thioanalogue bis(2-hydroxybenzaldehyde)thiocarbohydrazone (H_4L^S)

forms azine-bridged octanuclear copper(II) complexes.[22] The two reported 24-membered metallamacrocycles are unique examples where the ligands use their donor capacity in an unprecedented manner for thiocarbohydrazone coordination chemistry. In an attempt to enlarge this very small family of ligands we were interested to investigate whether related carbohydrazone ligands are also able to fully use their donor ability by deprotonation of dissociable functional groups and to compare the acid-base behaviour of H_4L and its thioanalogue H_4L^S. Herein we report on the experimental and calculated pK_a values for both H_4L and H_4L^S and on the synthesis of the products resulted from reactions of copper(II) nitrate and copper(II) sulfate with H_4L in DMSO/EtOH/H_2O, DMF/EtOH/H_2O or DMF/H_2O mixtures. The three isolated copper(II) complexes, namely $[Cu_2(HL)(DMSO)_2(H_2O)]NO_3 \cdot H_2O$ (**1**), $[\{Cu_2(HL)(DMF)(H_2O)\}_n][\{Cu_2(HL)(DMF)NO_3\}_n]$-$(NO_3)_n$ (**2**), and $[Cu_2(HL)(DMF)_2(H_2O)]HSO_4 \cdot H_2O$ (**3**), have been studied by elemental analysis, IR spectroscopy, magnetic and cyclic voltammetry measurements, as well as by X-ray crystallography, while $[Cu_2(HL)(DMF)_2(H_2O)][Cu_2(HL)(SO_4)(H_2O)(DMF)_2] \cdot 2H_2O$ (**4**) and $[Cu_4(HL)_2(HSO_4)(DMF)_2]HSO_4$ **(5)** only by X-ray crystallography.

Chart 1

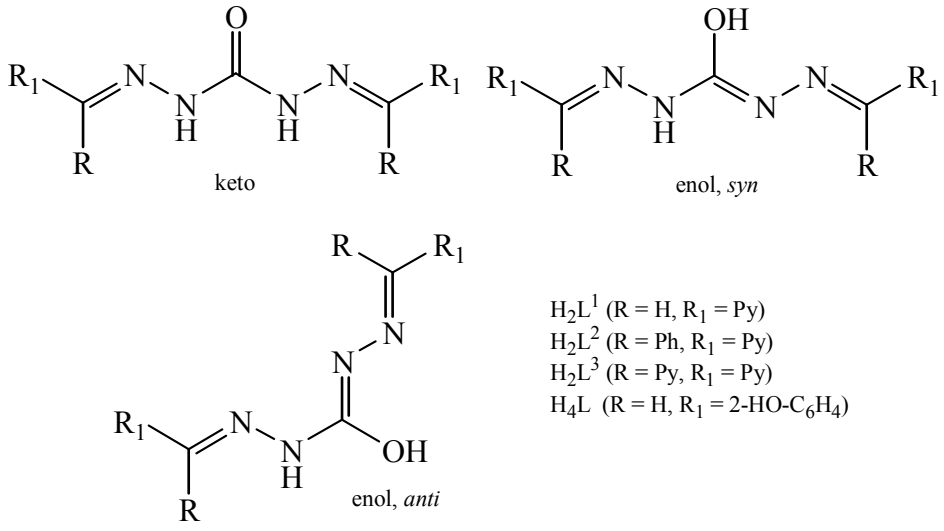

Experimental section

Materials. All reagents were used as received from Aldrich.

Synthesis of Ligands. 1,5-Bis(2-hydroxybenzaldehyde)carbohydrazone (H_4L) was prepared by a slight modification of the procedure reported previously.[23] Briefly, a mixture of 2-hydroxybenzaldehyde (1.1 ml, 10.0 mmol) in ethanol (20 mL) and carbohydrazide (0.45 g,

5.0 mmol) in water/ethanol 1:2 (20 ml) was refluxed for 1 h. The white solid formed was filtered off, washed with ethanol (5 ml), diethyl ether (5 ml) and dried in air. Yield: 1.42 g (90%). Anal. Calcd for $C_{15}H_{14}N_4O_3 \cdot H_2O$ (%): C, 56.96; H, 5.10; N, 17.71. Found, %: C, 56.83; H, 5.02; N, 18.16. 1,5-Bis(2-hydroxybenzaldehyde)thiocarbohydrazone (H_4L^S) was synthesised by following a literature protocol.[22]

Synthesis of complexes

$[Cu_2(HL)(DMSO)_2(H_2O)]NO_3 \cdot H_2O$ (1). To a solution of H_4L (0.15 g, 0.5 mmol) in ethanol/DMSO 5:1 (24 ml) was added $Cu(NO_3)_2 \cdot 3H_2O$ (0.24 g, 1.0 mmol) in water (5.0 ml). After 9 days a clear green solution produced green crystals, which were filtered off, washed with ethanol and dried in air. Yield: 0.15 g (44.4%). Anal. Calcd for $C_{19}H_{27}Cu_2N_5O_{10}S_2$ (M = 676.67 g/mol), %: C, 33.72; H, 4.02; N, 10.35. Found, %: C, 33.78; H, 3.92; N, 10.21. IR, ν, cm^{-1}: 1601 vs, 1494 vs, 1469 s, 1413 vs, 1385 vs, 1336 s, 1309 s, 1201 s, 1113 m, 1012 m, 954 m, 755 m, 735 m, 586 m, 564 m, 503 w, 471 w.

$[\{Cu_2(HL)(DMF)(H_2O)\}_n][\{Cu_2(HL)(DMF)NO_3\}_n](NO_3)_n$ (2). To a solution of H_4L (0.15 g, 0.5 mmol) in ethanol/DMF 5:1 (24 ml) was added $Cu(NO_3)_2 \cdot 3H_2O$ (0.24 g, 1.0 mmol) in water (5.0 ml). After 48 h a clear green solution produced green crystals, which were filtered off, washed with ethanol and dried at 130 °C for 1.5 h. Yield: 0.21 g (74.2%). Anal. Calcd for $C_{36}H_{38}Cu_4N_{12}O_{15}$ (M = 1132.94 g/mol), %: C, 38.16; H, 3.38; N, 14.84. Found: C, 38.49; H, 3.44; N, 14.79. IR, ν, cm^{-1}: 1597 vs, 1499 s, 1474 s, 1413 s, 1392 s, 1343 s, 1300 vs, 1279 vs, 1254 vs, 1205 vs, 1145 vs, 1063 s, 959 s, 908 s, 756 vs, 691 s, 620 s.

$[Cu_2(HL)(H_2O)(DMF)_2]HSO_4 \cdot H_2O$ (**3**). To a solution of H_4L (0.21 g, 0.7 mmol) in DMF (10 ml) was added $CuSO_4 \cdot 5H_2O$ (0.39 g, 1.4 mmol) in water (10 ml). After 2 days a clear green solution produced green crystals, which were filtered off, washed with ethanol and dried in air. Yield: 0.21 g (46.0%). Anal. Calcd for $C_{21}H_{29}Cu_2N_6O_{11}S$ (M = 700.65 g/mol), %: C, 36.00; H, 4.17; N, 11.99. Found: C, 36.04; H, 4.16; N, 11.91. IR, ν, cm^{-1}: 1643 vs, 1598 vs, 1538 m, 1500 vs, 1369 s, 1341 s, 1197 vs, 1144 vs, 1115 vs, 1037 vs, 864 s, 759 s, 695 s, 585 vs. If the reaction mixture is allowed to stand at room temperature over 7 days, at least two other complexes crystallize as minor species, namely $[Cu_2(HL)(DMF)_2(H_2O)]$ $[Cu_2(HL)(SO_4)(H_2O)(DMF)_2] \cdot 2H_2O$ (**4**) and $[Cu_4(HL)_2(HSO_4)(DMF)_2]HSO_4$ (**5**), as confirmed by X-ray crystallography.

Physical measurements. Infrared spectra were recorded on a Perkin Elmer Spectrum 100 FT-IR spectrometer. ESI mass spectra were recorded on a Bruker Esquire 3000 mass spectrometer by using methanol as solvent. The *m*/*z* values are quoted for the most intense peak in the isotopic pattern. Elemental analyses were performed at the Microanalytical Service of the Faculty of Chemistry of the University of Vienna.

UV–vis spectrophotometric and pH-potentiometric measurements. pH-Potentiometric measurements for determination of the pK_a values of H_4L and H_4L^S were carried out at 298.0 ± 0.1 K in DMSO/water 60:40 (w/w) as solvent at an ionic strength of 0.10 M (KCl, Sigma-Aldrich) in order to keep the activity coefficients constant. In addition, UV–vis spectrophotometric measurements were performed in DMSO/water 30:70 (w/w) as solvent with 0.10 M (KCl) ionic strength. All the titrations were performed with carbonate-free KOH (Sigma-Aldrich) solution of known concentration (0.10 M). An Orion 710A pH-meter equipped with a Metrohm combined electrode (type 6.0234.100) and a Metrohm 665 Dosimat burette were used for the measurements. The electrode system was calibrated to the pH = $\log[H^+]$ scale by means of blank titrations (strong acid vs strong base; HCl vs KOH) according to the method suggested by Irving *et al.*[24] The average water ionisation constant, pK_w, is 16.15 ± 0.01 in DMSO/water 60:40 (w/w) and 14.53 ± 0.05 in DMSO/water 30:70 (w/w) at 298 K, which corresponds well to the literature data.[25] Samples were deoxygenated by bubbling purified argon through the solutions for *ca.* 10 min prior to the measurements. Argon was also passed over the solutions during all kinds of titrations. The ligand concentration was 1 and 2 mM in the case of the pH-metric titrations in the 60% (w/w) DMSO/H_2O mixture over the pH range between 2 and 13.5.

A Hewlett Packard 8452A diode array spectrophotometer was used to record the UV–vis spectra in the interval 200 – 800 nm. The path length was 1 cm. The concentration of ligands was 0.025 mM in the 30% (w/w) DMSO/H_2O mixture over the pH range between 2 and 12.5. The initial volume of the samples was 10.00 mL. Proton dissociation constants of the ligands and the individual spectra of the species were calculated by the computer program PSEQUAD.[26]

Calculation of pK_a values of H_4L and H_4L^S. The gas-phase geometries of the isolated neutral H_4L and H_4L^S ligands[16] (Figure S1) as well as of their deprotonated $[H_nL]^{(4-n)-}$ and $[H_nL^S]^{(4-n)-}$ species, with n = 0, 1, 2 and 3, have been optimised. Experimental structures[16] have been used as the starting geometries without any conformational search for the sake of simplicity. In this way obtained structures have been re-optimised in aqueous solution by a standard Polarisable Conductor Calculation Model (CPCM) treatment using the radii from the UFF force field.[27,28] The stability of all optimised structures has been tested by vibrational analysis (no imaginary vibrations). All calculations have been performed at B3LYP/6-311++G** level of theory using Gaussian03 software.[29]

The pK_a value of the acid dissociation reaction[30,31,32,33]

$$HL \rightleftharpoons H^+ + L^- \qquad (1)$$

in an aqueous solution (subscript „aq") is defined as

$$pK_a = -\log K_a = \Delta G^*_{a,aq}/(2.303\ RT) \qquad (2)$$

where K_a is the equilibrium constant of the deprotonation reaction of the ligand (1), R is a universal gas constant, T is the absolute temperature and $\Delta G^*_{a,aq}$ is the corresponding free energy difference

$$\Delta G^*_{a,aq} = G^*(H^+_{aq}) + G^*(L^-_{aq}) - G^*(HL_{aq}) \qquad (3)$$

The superscript „*" represents a standard state of one mole per liter and T = 298.15 K in solution phase. Due to the unknown absolute free energy of the solvated proton $G^*(H^+_{aq})$ the eq. (3) is hardly usable. Nevertheless, the acid dissociation reaction (1) in gas phase (subscript „gas") and corresponding free energy change

$$\Delta G^o_{a,gas} = G^o(H^+_{gas}) + G^o(L^-_{gas}) - G^o(HL_{gas}) \qquad (4)$$

where the superscript "o" represents a standard state of a gas at standard pressure (1 atm) and T = 298.15 K with $G^o(H^+_{gas}) = -6.28$ kcal/mol (as obtained from Sackur-Tetrode equation at standard pressure and temperature) may be used for this purpose.[30,31,32,33] The transfer of X = HL, H^+ or L^- from gas to solvent is energetically characterised by the free energies of solvation

$$\Delta G_{solv}(X) = G^*(X_{aq}) - G^o(X_{gas}) \qquad (5)$$

Using a simple thermodynamic cycle with gas phase data,[30,31,32,33] $\Delta G^*_{a,aq}$ can be expressed as

$$\Delta G^*_{a,aq} = \Delta G^o_{a,gas} + \Delta\Delta G_{solv} + \Delta G^{o\rightarrow *} \qquad (6)$$

$$\Delta\Delta G_{solv} = \Delta G_{solv}(H^+) + \Delta G_{solv}(L^-) - \Delta G_{solv}(HL) \qquad (7)$$

where

$$\Delta G^{o\rightarrow *} = RT \ln 24.46 \quad (8)$$

is the free energy change associated with the change of standard state that uses the pressure of 1 atm in the ideal gas phase and 1 M in the aqueous phase, to a standard state that uses the concentration of 1 mol per liter in both the gas and aqueous phases ($\Delta G^{o\rightarrow *}$ amounts to 1.894 kcal/mol at 298 K). We then use these free energies ($G^{o}_{a,gas} + \Delta G_{solv}$), along with the literature value $\Delta G_{solv}(H^{+}) = -272.2$ kcal/mol[30,31,32,33] to compute the pK_a values using eqs. (2) and (6). We have calculated $\Delta G_{solv}(X)$ as the energy difference in the solution and gas phase for the optimal X geometry in solution.[30,31,32,33]

Muckerman et al.[30] found that in this way calculated p$K_{a,aq,calc}$ data suffer from a systematic error in the solvation model (especially for higher anion charges) and proposed a two-parametric linear scaling

$$pK_{a,aq,scal} = a + b\ pK_{a,aq,calc} \quad (9)$$

with a = 1.47 and b = 0.52 for B3LYP/6-311++G** level of theory and CPCM solvent treatment using the radii from the UFF force field. Alkorta et al.[33] successfully used analogous linear relation for the transfer of experimental pK_a values of carbon acids between aqueous and DMSO solutions.

Crystallography. The X-ray diffraction measurements were carried on a Bruker X8 APEXII (**1**, **2** and **4**) and Bruker D8 VENTURE (**3** and **5**) CCD diffractometers using graphite monochromated MoKα radiation (λ = 0.71073 Å) at 100(2) K. The data were processed using SAINT software.[34] The structures were solved by direct methods and refined by full-matrix least-squares techniques. Non-hydrogen atoms were refined with anisotropic displacement parameters. H atoms were placed at calculated positions and refined as riding atoms in the subsequent least-squares model refinements. The positional parameters of OH and NH hydrogen atoms were found from difference Fourier syntheses and verified by the geometric parameters of the corresponding hydrogen bonds. The following computer programs and hardware were used: SHELXS-97, SHELXL-97[35] and an Intel CoreDuo personal computer. Crystal data, data collection parameters, and structure refinement details for **1**−**5** are summarised in Table 1.

Magnetic susceptibility. The magnetic susceptibility data for all compounds were collected in a temperature range of 2 – 300 K under an applied field of 1 T on powdered microcrystalline samples with a SQUID magnetometer (MPMS-7, Quantum Design). Experimental susceptibility data were corrected for the underlying diamagnetism using Pascal's constants. The temperature dependent magnetic contribution of the holder was experimentally determined and subtracted from the measured susceptibility data. The resulting molar susceptibility data were plotted as $\chi_M T$ vs T. The program julX was used for spin Hamiltonian simulations of the data.[36]

Electrochemistry. Cyclic voltammetry (CV) experiments were performed at room temperature under an argon atmosphere by a HEKA potentiostat PG 390 using software package PotMaster v2x40 (HEKA Electronik, Germany). A standard three electrode arrangement of a platinum wire as the working electrode, a platinum wire as the counter electrode, and a silver wire as the pseudo-reference electrode was used. Solutions of copper(II) compexes **1**–**3** with an approximate concentration of 1 mM were prepared with 0.2 M tetrabutylammonium hexafluorophosphate ($TBAPF_6$) as a supporting electrolyte in dimethyl sulfoxide (DMSO) for **1** or in dimethylformamide (DMF) for **2** and **3**. Commercially available DMF, ferrocene (Fc) and decamethylferrocene (DmFc) purchased from Sigma-Aldrich and DMSO SeccoSolv® from Merck were used without further purification. $TBAPF_6$ of puriss quality (Fluka) was dried under reduced pressure at 70 °C for 24 h before use. The redox potentials are quoted against the decamethylferrocenium/decamethylferrocene couple ($DmFc^+$/DmFc). The $E_{1/2}(Fc^+/Fc)$ – $E_{1/2}(DmFc^+/DmFc)$ value of 0.54 V obtained in an independent experiment can be used to recalculate the sample redox potentials vs the Fc^+/Fc couple.

Table 1. Crystal data and details of data collection for **1 − 5**.

Compound	**1**	**2**	**3**	**4**	**5**
empirical formula	$C_{19}H_{27}Cu_2N_5O_{10}S_2$	$C_{36}H_{40}Cu_4N_{12}O_{16}$	$C_{21}H_{30}Cu_2N_6O_{11}S$	$C_{42}H_{58}Cu_4N_{12}O_{18}S$	$C_{36}H_{38}Cu_4N_{10}O_{16}S_2$
Fw	676.66	1150.96	701.65	1305.22	1185.04
space group	*P*-1	*P*-1	$P2_1/c$	*P*-1	$P2_1$/c
a [Å]	9.0876(3)	11.5114(4)	6.4293(7)	8.1559(3)	14.8807(4)
b [Å]	12.0905(4)	12.9844(5)	17.7216(17)	18.4762(6)	12.9381(3)
c [Å]	12.4374(5)	14.8967(5)	23.353(2)	19.4380(7)	22.3406(6)
α [°]	110.296(3)	88.466(2)		112.234(2)	
β [°]	90.753(2)	88.375(2)	95.830(3)	100.538(2)	107.6252(11)
γ [°]	97.863(2)	73.766(2)		101.540(2)	
V [Å^3]	1266.94(8)	2136.54(13)	2647.0(5)	2546.24(15)	4099.28(18)
Z	2	2	4	2	4
λ [Å]	0.71073	0.71073	0.71073	0.71073	0.71073
ρ_{calcd} [g cm^{-3}]	1.774	1.789	1.761	1.702	1.920
crystal size [mm]	0.22 × 0.08 × 0.06	0.20 × 0.08 × 0.02	0.09 × 0.02 × 0.02	0.4 × 0.12 × 0.01	0.09 × 0.07 × 0.01
T [K]	100(2)	100(2)	100(2)	100(2)	100(2)
μ [mm^{-1}]	1.907	2.051	1.757	1.774	2.238
R_1[a]	0.0251	0.0337	0.0660	0.0471	0.0338
wR_2[b]	0.0616	0.0884	0.1536	0.1443	0.0776
GOF[c]	1.052	1.037	1.058	1.069	1.008

[a] $R_1 = \Sigma||F_o| - |F_c||/\Sigma|F_o|$. [b] $wR_2 = \{\Sigma[w(F_o^2 - F_c^2)^2]/\Sigma[w(F_o^2)^2]\}^{1/2}$. [c] GOF = $\{\Sigma[w(F_o^2 - F_c^2)^2]/(n - p)\}^{1/2}$, where *n* is the number of reflections and *p* is the total number of parameters refined.

2. Results and discussion

Synthesis. The 1,5-bis(2-hydroxybenzaldehyde)carbohydrazone (H_4L) was prepared by heating 2-hydroxybenzaldehyde with carbohydrazide in 2:1 molar ratio in ethanol/water (~ 4:1). Reaction of $Cu(NO_3)_2{\cdot}3H_2O$ with H_4L in ethanol/DMSO/water 5:1:1.25 at room temperature produced green crystals of $[Cu_2(HL)(DMSO)_2(H_2O)]NO_3{\cdot}H_2O$ (**1**), which were separated after 9 days in 44% yield. If a mixture of ethanol/DMF/water 5:1:1.25 is used as solvent the reaction mixture generates green crystals of the composition $[\{Cu_2(HL)(DMF)(H_2O)\}_n][\{Cu_2(HL)(DMF)NO_3\}_n](NO_3)_n$ (**2**), which were isolated after 2 days in 74% yield. Starting from $CuSO_4{\cdot}5H_2O$ and H_4L in 2:1 molar ratio in DMF/water 1:1 green crystals of $[Cu_2(HL)(H_2O)(DMF)_2]HSO_4{\cdot}H_2O$ (**3**) were obtained at room temperature and separated after 2 days in 46% yield. If the reaction mixture was allowed to stand at room temperature over 7 days, the formation of additional minor species was observed and confirmed by X-ray diffraction, namely green-blue crystals of the composition $[Cu_2(HL)(DMF)_2(H_2O)][Cu_2(HL)(SO_4)(H_2O)(DMF)_2]{\cdot}2H_2O$ (**4**) and green crystals of $[Cu_4(HL)_2(HSO_4)(DMF)_2]HSO_4$ (**5**). The complexes **4** and **5** could not be accumulated and isolated as pure compounds in sufficient amounts for further investigations both in the solid state and in solution. The ESI mass spectra of **1**–**3** in methanol recorded in positive ion mode showed intense peaks at *m/z* 421 and 843 attributable to $[Cu_2(HL)]^+$ and $[\{Cu_2(HL)\}_2{-}H^+]^+$, respectively. The experimental isotopic patterns fit perfectly those calculated for the two ions. In addition, strong peaks at *m/z* 1265 for **2** and 1363 for **3** due to $[\{Cu_2(HL)_3\}_3{-}2H^+]^+$ and $[\{Cu_2(HL)_3\}_3(SO_4)]^+$, respectively, were found. Their relative intensities do not vary with dilution. Fragmentation of $[\{Cu_2(HL)_3\}_3(SO_4)]^+$ in ms/ms spectra also confirms the assignment of ions and the formation of trimeric associates in methanolic solution of **3**. Moreover tetrameric associates $[\{Cu_2(HL)\}_4{-}3H^+]^+$ and $[\{Cu_2(HL)\}_4(SO_4)\ {-}H^+]^+$ were observed respectively at *m/z* 1685 for **1**, **2** and 1785 for **3**.

pK_a values of H_4L and H_4L^S. The deprotonation processes of H_4L and H_4L^S were followed by pH-potentiometry in DMSO/H_2O 60:40 mixture. The ligands have limited solubility at the concentration levels necessary for pH-potentiometric titrations (i.e. ≥1–2 mM) in the 30:70 DMSO/H_2O medium. Therefore, UV–vis spectrophotometric titrations have been performed only in highly diluted solutions (25 μM). The low solubility of both H_4L and H_4L^S did not allow using these methods for pure aqueous solutions. Although the studied ligands contain 4

dissociable groups (2 phenolic OH and 2 hydrazinic NH) the pH-metric measurements and the recorded pH-dependent spectra (Figures 1a and S2a) revealed only two proton dissociation processes and the macroscopic pK_a values are quoted in Table 2.

Table 2. Proton dissociation constants (pK_a) of ligand H_4L and its thioanalogue (H_4L^S) determined by pH-potentiometry in 60% (w/w) DMSO/H_2O and by UV−vis spectrophotometry in 30% (w/w) DMSO/H_2O together with the estimated values for the pure aqueous phase from the pK_a values measured in the DMSO/H_2O mixtures with the help of the slopes of the pK_a vs $1/\varepsilon_r$ curves {T = 298 K, I = 0.10 M KCl}[a].

	0% (w/w)	30% (w/w)	60% (w/w)
H_4L pK_1	9.17	9.35(2)	9.87(6)
H_4L pK_2	10.23	10.52(2)	11.36(8)
H_4L^S pK_1	6.12	6.71(2)	8.41(4)
H_4L^S pK_2	10.06	10.49(1)	11.75(3)

[a] Standard deviations (SD) in parenthesis.

Both deprotonation steps of the ligands H_4L and H_4L^S were accompanied by characteristic spectral changes in the pH-dependent UV−vis spectra (Figures 1a and S2a). The absorption bands of the individual ligand species (H_4L, H_3L^- and H_2L^{2-}) were calculated on the basis of deconvolution of the spectra (Figures 1b and S2b). The first proton dissociation process results in the development of a strong band at λ_{max} = 364 nm and 372 nm in the case of H_4L and H_4L^S, respectively. Similar spectral changes were assigned to the deprotonation of the phenolic moiety for the structurally analogous reference compounds, namely salicylaldehyde semicarbazone (SSC) and thiosemicarbazone (STSC).[37,38] This finding strongly suggests that pK_1 belongs mostly to the deprotonation of one of the phenolic groups. However, this is in contrast with the theoretical calculations (vide infra). pK_1 of H_4L is almost identical to that of SSC (9.32) measured in 30% (w/w) DMSO/H_2O. On the other hand pK_1 of H_4L^S is lower by more than one order of magnitude compared to that of STSC (8.89), which is presumably due to a different arrangement of the functional groups in the two molecules. It is noteworthy that the dissociation steps are overlapping, especially in the case of H_4L. In the second deprotonation step the λ_{max} values are increased only by ~10 nm. This can be the result of the deprotonation of another PhOH or one of the hydrazinic groups, although, the pK_a of the

hydrazinic group of the STSC is 12.59 and even much higher for SSC in the 30% (w/w) DMSO/H_2O mixture.[37,38]

Additionally, both pK_a values of the ligands are decreased if the DMSO content in the solvent mixture is diminished (Table 2), which corresponds well to the expectations based on the Born electrostatic solvent model,[39] namely the pK_a of the anionic bases (such as the phenolate groups) is increased in the presence of DMSO compared to pure water due to the charge neutralisation by protonation. Therefore, the pK_a values obtained in the 30% and 60% (w/w) DMSO/H_2O mixtures were plotted against the reciprocal value of the relative permittivity (or dielectric constant, ε_r) of the medium (Figure 2) and on the basis of the negative slopes pK_a of both ligands in pure aqueous phase were extrapolated from the values obtained in the DMSO/H_2O mixtures (Table 2). Based on these data it can be concluded that the studied carbohydrazone (H_4L) and the thiocarbohydrazone (H_4L^S) exhibit significantly different pK_1 values which can bring somewhat easier complex formation with H_4L^S.

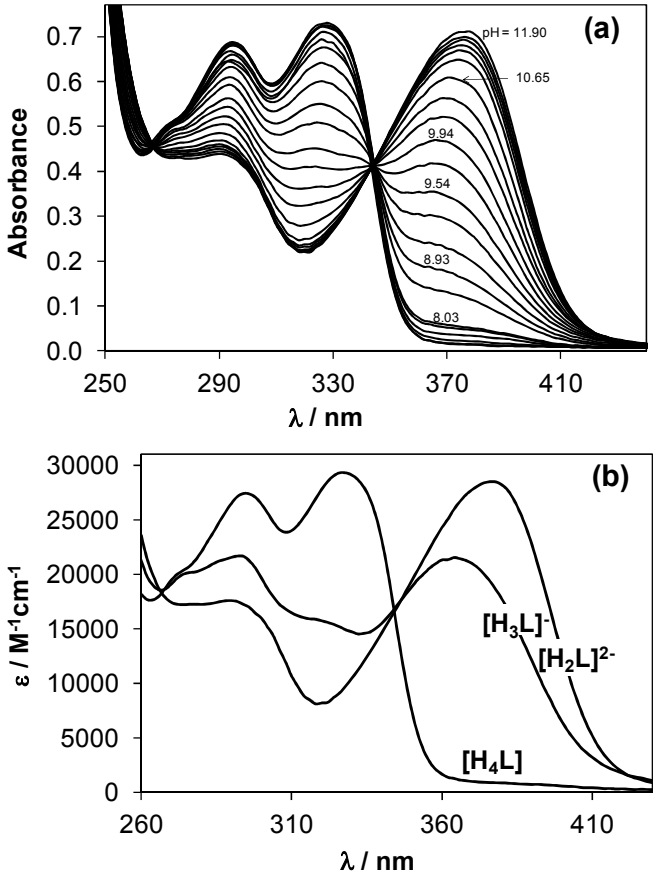

Figure 1. UV–vis absorption spectra of the ligand H_4L recorded at pH values from 3.0 to 11.90 (a) and calculated individual absorption spectra for ligand species (b). {c_{ligand} = 25 μM; 30% (w/w) DMSO/H_2O; T = 298 K, I = 0.1 M (KCl)}.

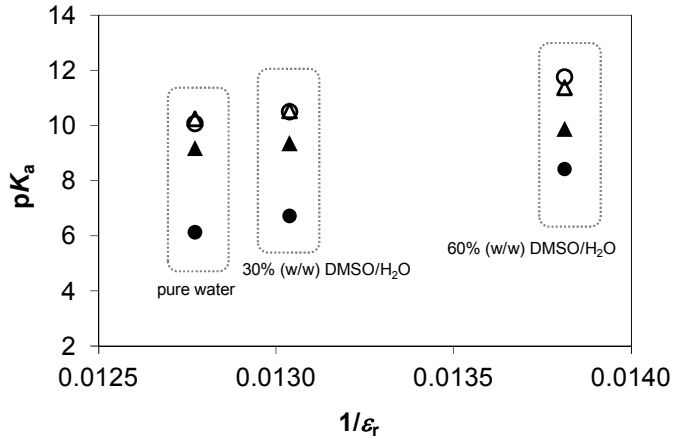

Figure 2. Correlation diagram for the pK_a values measured at various DMSO content plotted against the $1/\varepsilon_r$ values of the solvent medium for H_4L (pK_1: ▲; pK_2: Δ) and H_4L^S (pK_1: •; pK_2: ◦) {I = 0.10 M (KCl) in 30 and 60% (w/w) DMSO/H_2O}. ε_r values are interpolated data taken from ref. 40. ε_r = 78.3 for H_2O, 76.7 for 30% and 72.4 for 60% (w/w) DMSO/H_2O mixtures.

Calculated pK_a values of H_4L and H_4L^S. The H_4L and H_4L^S ligands have crystallographic twofold rotation symmetry (see Figure S1).[16] Two hydrazinic protons (H_N and $H_{N'}$) as well as the two phenolic ones (H_O and $H_{O'}$), which may be released, are symmetry related. This reduces the number of deprotonated $[H_nL]^{(4-n)-}$ and $[H_nL^S]^{(4-n)-}$ species, n = 0, 1, 2 and 3 (see Table 3).

Our results indicate that in the first step the deprotonation of the hydrazinic group is preferred over that of the phenolic one. This can be explained by O–H···N hydrogen bonding. The measured pK_1 values of both ligands exhibit the same trend as the calculated ones for the first deprotonation of their hydrazinic groups (compare Tables 2 and 4). In the second step surprisingly the deprotonation of the opposite hydrazinic and phenolic groups is mostly advantageous in spite of the above mentioned hydrogen bonding. Unlike $[H_2L]^{2-}$, in the case of $[H_2L^S]^{2-}$ the next preferred deprotonation sites are the hydrazinic ones. Due to a very complex deprotonation equilibria we are not able to compare the measured pK_2 values with their calculated counterparts. In the third step the deprotonation of both OH groups and a single hydrazinic group is preferred over the opposite case for both ligands. The deprotonation site can be changed by the solvent effect as well (see the doubly deprotonated species in Table 3). It is evident that the energy changes between deprotonated species increase with the degree of deprotonation.

Table 3. Calculated free energy data of the systems under study in vacuum ($G^{o}_{a,gas}$), solvation free energy in aqueous solution (ΔG_{solv}) and their summation at room temperature (bold denotes the preferred deprotonated species).

Microspecies	$G^{o}_{a,gas}$ [hartree]	ΔG_{solv} [hartree]	$G^{o}_{a,gas}$ + ΔG_{solv} [hartree]
$[LH_OH_O,H_NH_{N'}]^0$	−1024.730049	–0.029097	−1024.759146
$[LH_OH_NH_{N'}]^-$	−1024.184341	–0.109182	−1024.293523
$[LH_OH_O,H_N]^-$	**−1024.221258**	**–0.081647**	**−1024.302906**
$[LH_OH_{N'}]^{2-}$	**−1023.578755**	**–0.251804**	**−1023.830559**
$[LH_OH_N]^{2-}$	−1023.555910	–0.267989	−1023.823894
$[LH_NH_{N'}]^{2-}$	−1023.564747	–0.260446	−1023.825193
$[LH_OH_O]^{2-}$	−1023.571018	–0.251322	−1023.822340
$[LH_N]^{3-}$	**−1022.834720**	**–0.513584**	**−1023.348304**
$[LH_O]^{3-}$	−1022.811111	–0.527101	−1023.338212
$[L]^{4-}$	−1021.988122	–0.872080	−1022.860202
$[L^SH_OH_O,H_NH_{N'}]^0$	−1347.684645	–0.030185	−1347.714830
$[L^SH_OH_NH_{N'}]^-$	−1347.141304	–0.108407	−1347.249711
$[L^SH_OH_O,H_N]^-$	**−1347.185550**	**–0.082816**	**−1347.268366**
$[L^SH_OH_{N'}]^{2-}$	**−1346.543593**	**–0.253139**	**−1346.796732**
$[L^SH_OH_N]^{2-}$	−1346.526741	–0.265730	−1346.792471
$[L^SH_NH_{N'}]^{2-}$	−1346.521338	–0.261068	−1346.782406
$[L^SH_OH_O]^{2-}$	−1346.543041	–0.252700	−1346.795741
$[L^SH_N]^{3-}$	**−1345.805474**	**–0.513118**	**−1346.318592**
$[L^SH_O]^{3-}$	−1345.789249	–0.525004	−1346.314253
$[L^S]^{4-}$	−1344.964734	–0.856984	−1345.821718

Table 4. Calculated free energies of the individual acid dissociation reactions ($\Delta G^*_{a,aq}$), their calculated ($pK_{a,aq,calc}$) and scaled ($pK_{a,aq,scal}$) pK_a values of the microspecies of H_4L and H_4L^S in aqueous solutions and scaled pK_a values transferred to DMSO solutions ($pK_{a,DMSO,scal}$).

Equilibrium	$\Delta G^*_{a,aq}$ (kcal/mol)	$pK_{a,aq,calc}$	$pK_{a,aq,scal}$	$pK_{a,DMSO,scal}$
$[LH_OH_O,H_NH_{N'}]^0 \rightleftharpoons H^+ + [LH_OH_NH_{N'}]^-$	17.533	12.85	8.15	16.16
$[LH_OH_O,H_NH_{N'}]^0 \rightleftharpoons H^+ + [LH_OH_{O'},H_N]^-$	11.645	8.53	5.91	12.87
$[LH_OH_NH_{N'}]^- \rightleftharpoons H^+ + [LH_OH_{N'}]^{2-}$	15.864	11.63	7.52	15.22
$[LH_OH_NH_{N'}]^- \rightleftharpoons H^+ + [LH_OH_N]^{2-}$	20.047	14.69	9.11	17.56
$[LH_OH_NH_{N'}]^- \rightleftharpoons H^+ + [LH_NH_{N'}]^{2-}$	10.405	7.63	5.44	12.18
$[LH_OH_O,H_N]^- \rightleftharpoons H^+ + [LH_OH_{N'}]^{2-}$	21.752	15.94	9.76	18.51
$[LH_OH_O,H_N]^- \rightleftharpoons H^+ + [LH_OH_N]^{2-}$	25.935	19.01	11.35	20.84
$[LH_OH_O,H_N]^- \rightleftharpoons H^+ + [LH_OH_{O'}]^{2-}$	26.910	19.72	11.73	21.39
$[LH_OH_{N'}]^{2-} \rightleftharpoons H^+ + [LH_N]^{3-}$	27.970	20.50	12.13	21.98
$[LH_OH_{N'}]^{2-} \rightleftharpoons H^+ + [LH_O]^{3-}$	34.302	25.14	14.54	25.51
$[LH_OH_N]^{2-} \rightleftharpoons H^+ + [LH_N]^{3-}$	23.787	17.43	10.54	19.64
$[LH_OH_N]^{2-} \rightleftharpoons H^+ + [LH_O]^{3-}$	30.120	22.07	12.95	23.18
$[LH_NH_{N'}]^{2-} \rightleftharpoons H^+ + [LH_N]^{3-}$	33.429	24.50	14.21	25.02
$[LH_OH_{O'}]^{2-} \rightleftharpoons H^+ + [LH_O]^{3-}$	29.145	21.36	12.58	22.63
$[LH_N]^{3-} \rightleftharpoons H^+ + [L]^{4-}$	31.639	23.19	13.53	24.02
$[LH_O]^{3-} \rightleftharpoons H^+ + [L]^{4-}$	25.306	18.55	11.11	20.49
$[L^SH_OH_O,H_NH_{N'}]^0 \rightleftharpoons H^+ + [L^SH_OH_NH_{N'}]^-$	17.217	12.62	8.03	15.98
$[L^SH_OH_O,H_NH_{N'}]^0 \rightleftharpoons H^+ + [L^SH_OH_{O'},H_N]^-$	5.510	4.04	3.57	9.45
$[L^SH_OH_NH_{N'}]^- \rightleftharpoons H^+ + [L^SH_OH_{N'}]^{2-}$	9.599	7.03	5.13	11.73
$[L^SH_OH_NH_{N'}]^- \rightleftharpoons H^+ + [L^SH_OH_N]^{2-}$	12.272	8.99	6.15	13.22
$[L^SH_OH_NH_{N'}]^- \rightleftharpoons H^+ + [L^SH_NH_{N'}]^{2-}$	18.588	13.62	8.55	16.74
$[L^SH_OH_O,H_N]^- \rightleftharpoons H^+ + [L^SH_OH_{N'}]^{2-}$	21.305	15.61	9.59	18.26
$[L^SH_OH_O,H_N]^- \rightleftharpoons H^+ + [L^SH_OH_N]^{2-}$	23.979	17.57	10.61	19.75
$[L^SH_OH_O,H_N]^- \rightleftharpoons H^+ + [L^SH_OH_{O'}]^{2-}$	21.927	16.07	9.83	18.61
$[L^SH_OH_{N'}]^{2-} \rightleftharpoons H^+ + [L^SH_N]^{3-}$	25.387	18.61	11.14	20.54
$[L^SH_OH_{N'}]^{2-} \rightleftharpoons H^+ + [L^SH_O]^{3-}$	28.110	20.60	12.18	22.06
$[L^SH_OH_N]^{2-} \rightleftharpoons H^+ + [L^SH_N]^{3-}$	22.714	16.65	10.13	19.04
$[L^SH_OH_N]^{2-} \rightleftharpoons H^+ + [L^SH_O]^{3-}$	25.436	18.64	11.16	20.56
$[L^SH_NH_{N'}]^{2-} \rightleftharpoons H^+ + [L^SH_N]^{3-}$	16.398	12.02	7.72	15.52
$[L^SH_OH_{O'}]^{2-} \rightleftharpoons H^+ + [L^SH_O]^{3-}$	27.488	20.15	11.95	21.71
$[L^SH_N]^{3-} \rightleftharpoons H^+ + [L^S]^{4-}$	37.143	27.22	15.62	27.09
$[LH_O]^{3-} \rightleftharpoons H^+ + [L]^{4-}$	34.420	25.23	14.59	25.58

We have applied the above mentioned pK_a calculations to the deprotonation of anionic $[H_nL]^{(4-n)-}$ and $[H_nL^S]^{(4-n)-}$ species despite the method[30,31,32] has been originally developed for neutral acids. The calculated and scaled pK_a values in aqueous solutions differ

significantly (compare $pK_{a,aq,calc}$ and $pK_{a,aq,scal}$ in Table 4) but the scaled values should better agree with the experimental ones (Table 2). It should be noted that pK_a values determined by the calculations are microconstants providing a deeper knowledge about the proton dissociation processes of the various microspecies, while the experimentally determined pK_a values obtained by *e.g.* pH-potentiometry can give phenomenological information in the pH-range studied. The microconstants also suggest the overlapping deprotonation of the dissociable groups and are generally lower for the deprotonation of the phenolic groups compared with hydrazinic protons. For the comparison with the values obtained from mixed DMSO/H_2O solutions we have used a linear transformation

$$pK_{a,DMSO,scal} = c + d\ pK_{a,aq,scal} \qquad (10)$$

where the coefficients c = 4.22±0.51 and d = 1.464±0.060 (with R-squared = 0.9967, std. deviation = 0.92, n = 6) have been obtained by the linear regression of the experimental $pK_{a,aq}$ values of the compounds in the training set of Muckerman et al.[30] for which the analogous $pK_{a,DMSO}$ values are known[41] (see Table S1 and Figure S3 in Supplementary Information). Our coefficients are very similar to those obtained by Alkorta et al.[33] for carbon acids. The measured pK_a values in various aqueous-DMSO solutions should correspond to the linear combinations of $pK_{a,aq}$ and $pK_{a,DMSO}$ values.

Crystal Structures

$[Cu_2(HL)(DMSO)_2(H_2O)]NO_3 \cdot H_2O$ (1). A view of the asymmetric unit in the crystal structure of **1** is shown in Figure 3, while selected bond distances and bond angles are quoted in Table 5.

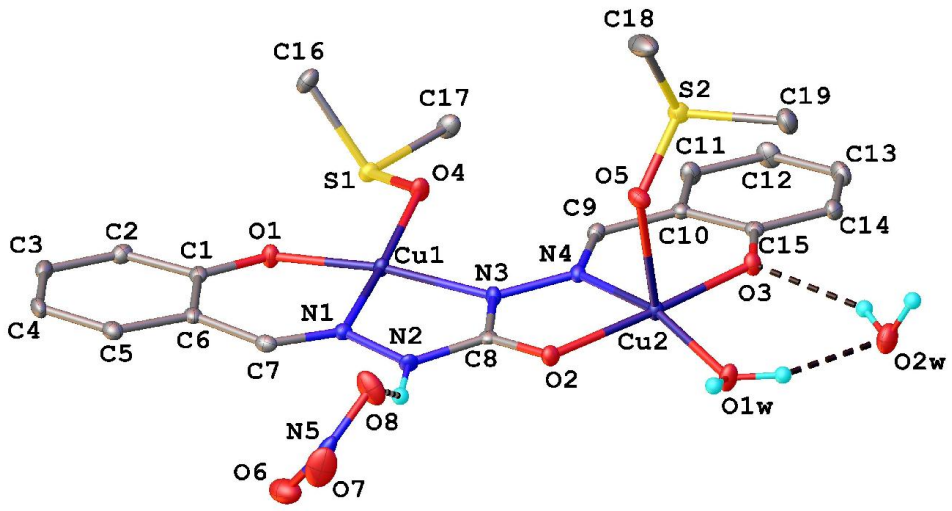

Figure 3. ORTEP view of the asymmetric unit in **1** with thermal ellipsoids drawn at 40% probability level. Hydrogen atoms were omitted for clarity.

Table 5. Selected bond distances (Å) and angles (°) in **1**.

Cu1–O1	1.882(2)	Cu2–O1*w*	1.957(2)
Cu1–O4	1.946(2)	N1–N2	1.384(2)
Cu1–N1	1.928(2)	N2–C8	1.363(3)
Cu1–N3	1.978(2)	C8–O2	1.264(2)
Cu2–N4	1.932(2)	C8–N3	1.343(3)
Cu2–O3	1.911(2)	N3–N4	1.397(2)
Cu2–O2	1.971(2)	C7–N1	1.290(3)
Cu2–O5	2.318(2)	C9–N4	1.288(3)

O1Cu1O4	88.38(6)	O1*w*Cu2O3	91.51(6)
O1Cu1N1	92.90(7)	O1*w*Cu2N4	164.75(7)
O1Cu1N3	172.02(7)	O3Cu2O2	175.26(6)
O4Cu1N3	97.90(7)	O3Cu2O5	95.49(6)
N1Cu1O4	172.39(7)	O3Cu2N4	93.42(7)
N1Cu1N3	81.53(7)	O2Cu2O5	85.65(6)
O1*w*Cu2O2	92.97(6)	O2Cu2N4	81.85(7)
O1*w*Cu2O5	95.09(6)	O5Cu2N4	98.78(6)

Two copper(II) atoms, one square-planar Cu1 and the other square-pyramidal Cu2 (τ_5 = 0.18),[42] are bridged by the N-N diazine fragment of the hexadentate ligand with a Cu1···Cu2 separation of 4.7673(4) Å. The Cu–N–N–Cu torsional angle is of 168.8(1)º. Cu1 and Cu2 atoms accommodated in ONN and ONO ligand pockets, respectively, require additional ligands (DMSO or DMSO and H_2O) to complete their coordination spheres. The triply deprotonated ligand HL^{3-} is bound to two divalent metal ions with formation of a dicopper(II) unit $\{Cu_2(HL)\}^+$. Its positive charge is counterbalanced by the nitrate anion. The C8−O2 bond length increases from 1.217(3) Å in the copper-free ligand to 1.264(3) Å in **1**, and the C−N bond shortens from 1.375(2) Å to 1.343(3) Å, indicating that the ligand adopts the enolate tautomeric form. Due to the numerous hydrogen bonds, which are evident in the crystal, two complex cations $[Cu_2(HL)(DMSO)_2(H_2O)]^+$ and two NO_3^- anions are assembled into a centrosymmetric tetranuclear associate, as shown in Figure 4. The hydrogen bonding parameters are listed in Table S2. The π-π stacking interaction at 3.871 Å for centroid-to-centroid separation and 1.750 Å for shift distance between adjacent H-bonded entities leads to the formation of supramolecular bands (Figure S4), which run parallel to the *c* crystallographic axis.

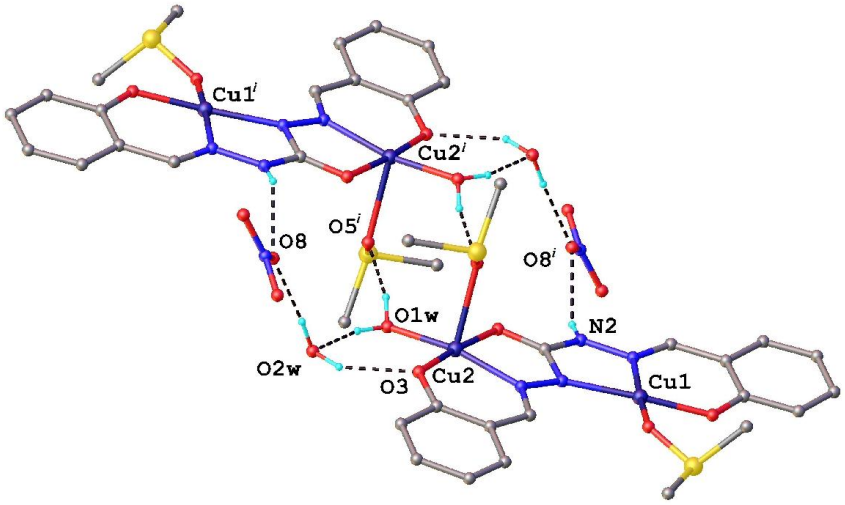

Figure 4. Hydrogen bonded dimeric associate in **1**.

[{Cu_2(HL)(DMF)(H_2O)}$_n$][{Cu_2(HL)(DMF)NO_3}$_n$](NO_3)$_n$ (2). Crystal structure analysis revealed that **2** consists of two different tetranuclear planar cationic and neutral units {[Cu_2(HL)(DMF)(H_2O)]$^+$}$_2$ (Figure 5a) and {[Cu_2(HL)(DMF)NO_3]}$_2$ (Figure 5b). Selected bond distances and bond angles are quoted in Table 6. Both units lie on the inversion centres with the Cu···Cu separations of 2.9686(8) and 2.9665(8) Å for the phenolate oxygen bridged pairs, Cu2A···Cu2A^i, Cu2B···Cu2B^i, and 4.8027(6) and 4.7990(6) Å for N−N bridged pairs, Cu1A···Cu2A, Cu1B···Cu2B, respectively. The Cu1A–N3A–N4A–Cu2A, and Cu1B–N3B–N4B–Cu2B torsion angles are at 179.6(2) and 172.3(2)º, respectively. The Cu2A and Cu2B atoms are square-pyramidal (τ_5 = 0.15 and 0.10, respectively) bound to ONO donors of the ligand HL^{3-} and a phenolate oxygen atom from another ligand. The apical site is occupied by the nitrato ligand or water molecule (Figure S5). These units in turn are linked through the phenolate atoms O1A and O1B to form stepped polymeric chains via a centre of inversion, giving Cu···Cu separations of 3.2617(7) and 3.2489(7) Å (Figure S5). The Cu1A and Cu1B atoms are coordinated by the other, ONN donor site of the ligand. The fourth coordination places in the basal planes are occupied by the oxygen atoms of DMF molecules. The symmetry-related phenolate O atoms occupy the apical positions of the resulting square-pyramids, and the bridging Cu–$O_{phenolate}$ bonds are significantly longer (Cu1A−O1A^i 2.483(2), Cu1B−O1B^i 2.468(2) Å) than the Cu−O1 (1.913(2), 1.915(2) Å for **A** and **B**, respectively) and the Cu2−O3 bonds [1.987(2), 1.972(2) Å for **A** and **B**, respectively]. In the crystal structure the both above mentioned stepped polymeric chains are strongly interacting via N−H···O and O−H···O intermolecular hydrogen bonds involving NH groups

and coordinated water molecules as proton donors and co-crystallised water molecules and NO_3^- counterions as proton acceptors. As a result, the main crystal packing motif can be characterised as a 3D supramolecular aggregate, as shown in Figure S6. Details of the hydrogen bonding parameters are given in Table S2.

a)

b)

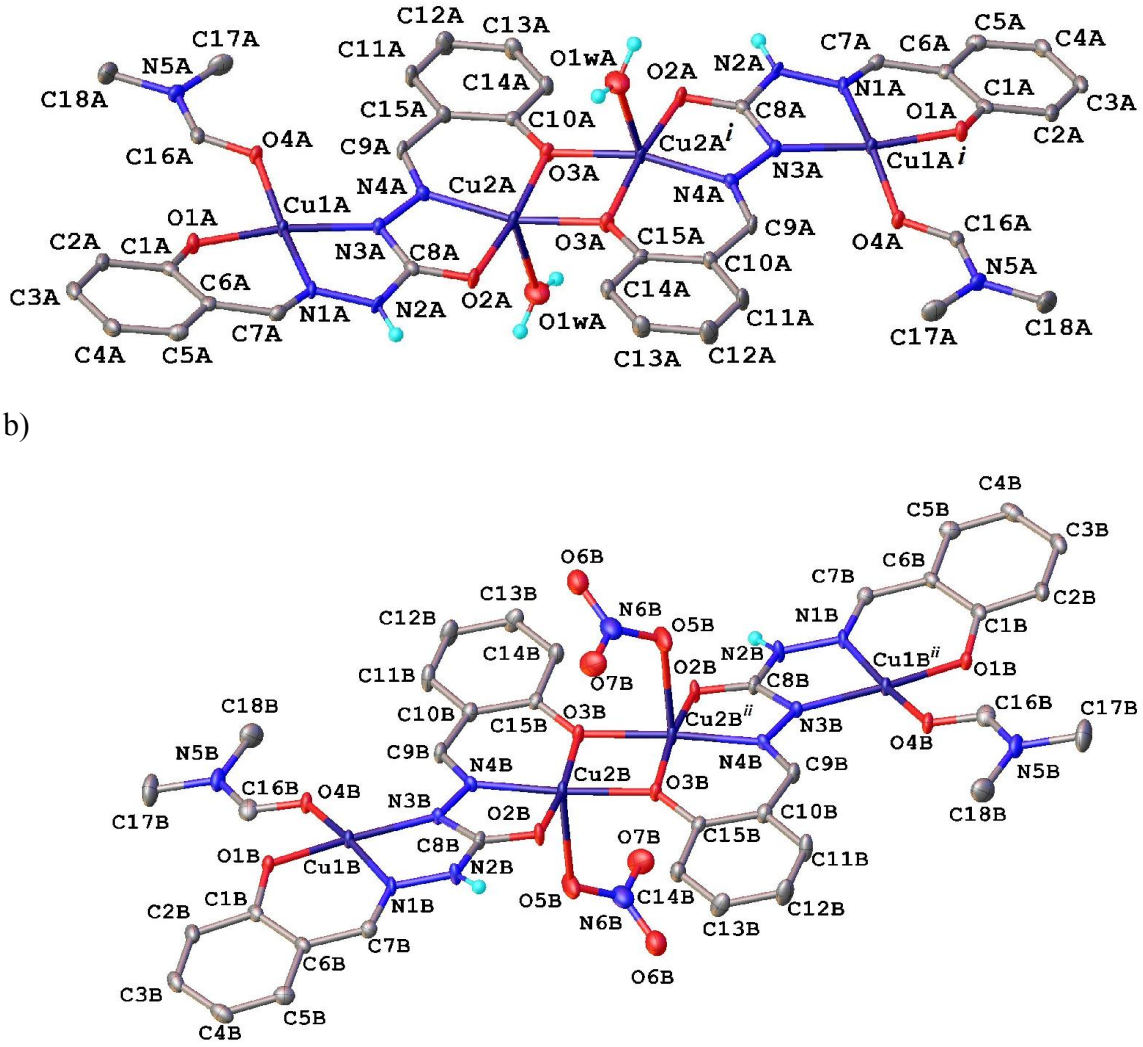

Figure 5. ORTEP views of a) $\{[Cu_2(HL)(DMF)(H_2O)]^+\}_2$ and b) $\{[Cu_2(HL)(DMF)NO_3]\}_2$ in **2**. Thermal ellipsoids are drawn at 50% probability level. Symmetry codes: (*i*) $-x, 2-y, 1-z$; (*ii*) $2-x, -y, -z$

Table 6. Selected bond distances (Å) and angles (deg) in **2**.

	A	**B**
Cu1–O1	1.913(2)	1.915(2)
Cu1–O4	1.982(2)	1.974(2)

Cu1–N1	1.956(3)	1.954(3)
Cu1–N3	1.995(3)	1.999(3)
Cu2–O1*w*	2.286(2)	-
Cu2–O2	1.918(2)	1.935(2)
Cu2–O3	1.914(2)	1.923(2)
Cu2–O3^{i}	1.987(2)	1.972(2)
Cu2–N4	1.944(3)	1.940(3)
Cu2–O5	-	2.363(2)
N1–N2	1.383(3)	1.375(3)
N2–C8	1.369(4)	1.364(4)
C8–O2	1.273(4)	1.263(4)
C8–N3	1.323(4)	1.344(4)
N3–N4	1.395(4)	1.392(3)
C7–N1	1.289(4)	1.288(4)
C9–N4	1.284(4)	1.280(4)

O1Cu1O4	90.22(9)	90.57(9)
O1Cu1N1	90.5(1)	89.9(1)
O1Cu1N3	170.7(1)	170.5(1)
O4Cu1N3	98.8(1)	98.8(1)
N1Cu1O4	170.26(9)	171.60(9)
N1Cu1N3	80.9(1)	81.1(1)
O2Cu2O1w	99.62(9)	
O2Cu2O3^{i}	102.12(9)	103.34(9)
O2Cu2N4	81.8(1)	81.8(1)
O3Cu2O1*w*	87.58(9)	
O3^{i}Cu2O1*w*	89.55(9)	
O3Cu2O2	172.15(9)	168.62(9)
O3Cu2O3^{i}	80.92(9)	80.80(9)
O3Cu2N4	93.3(1)	93.8(1)
N4Cu2O1*w*	106.1(1)	
N4Cu2O3^{i}	163.10(9)	174.4(1)
O2Cu2O5		94.16(9)
O3Cu2O5		96.73(9)
O3^{i}Cu2O5		85.86(8)
N4Cu2O5		96.07(9)

[Cu_2(HL)(H_2O)$(DMF)_2$]HSO_4·H_2O (3). The crystal of **3** is built up from dinuclear cationic units [Cu_2(HL)(H_2O)$(DMF)_2$]$^+$, HSO_4^- counterions and co-crystallised water molecules in 1:1:1 ratio, as shown in Figure 6. In the dinuclear unit Cu1 and Cu2 atoms coordinated respectively by ONN and ONO donor atom sets of the triply deprotonated hexadentate ligand HL^{3-} are bridged by diazine fragment with Cu1···Cu2 separation of 4.782(1) Å and Cu1–N3–N4–Cu2 torsion angle of 177.8(3)º. The square-planar and square-pyramidal

coordination polyhedra for Cu1 and Cu2 (τ_5 = 0) atoms are completed by DMF and by DMF and H_2O as monodentate ligands, respectively. The interatomic distances which are quoted in Table 7 indicate that the Schiff base ligand is in the enolate form, as observed for above described complexes. Two adjacent centrosymetrically related complex cations are interacting through hydrogen bonds between the coordinated water molecules as proton donors and coordinated phenolate and DMF oxygen atoms as proton acceptors, resulting in the formation of a tetranuclear supramolecular unit, as shown in Figure S7. The Cu2···Cu2^{i} separation is of 4.846(2) Å. In the crystal structure these tetranuclear units are further interacting through N–H···O and O–H···O hydrogen bonds (Table S2) with the participation of HSO_4^- counterions and noncoordinated water molecules. The formation of two-dimensional supramolecular layers running parallel to *ab* plane is shown in Figure S8.

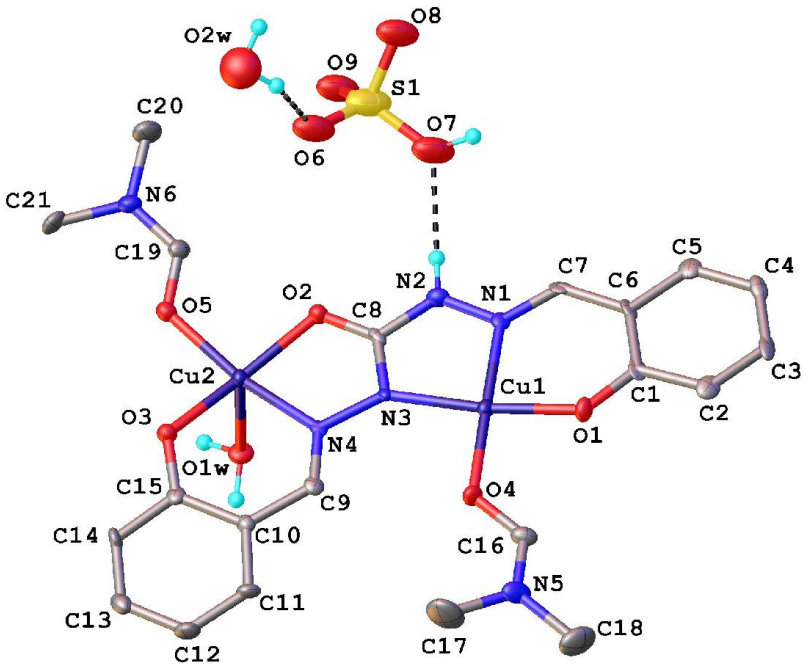

Figure 6. ORTEP view of $[Cu_2(HL)(H_2O)(DMF)_2]HSO_4 \cdot H_2O$ (**3**) with thermal ellipsoids drawn at 50% probability level.

Table 7. Selected bond distances (Å) and angles (deg) in **3**.

Cu1–O1	1.882(4)	Cu2–N4	1.942(5)
Cu1–O4	1.958(4)	N1–N2	1.354(7)
Cu1–N1	1.959(5)	N2–C8	1.365(8)
Cu1–N3	1.978(5)	C8–O2	1.263(7)
Cu2–O1*w*	2.271(4)	C8–N3	1.329(7)
Cu2–O2	1.948(4)	N3–N4	1.395(7)
Cu2–O3	1.895(4)	C7–N1	1.287(8)
Cu2–O5	1.970(4)	C9–N4	1.268(7)

O1Cu1O4	87.8(2)	O3Cu2O1*w*	92.0(2)
O1Cu1N1	91.7(2)	O3Cu2O2	168.8(2)
O1Cu1N3	173.0(2)	O3Cu2O5	90.3(2)
O4Cu1N3	98.9(2)	O3Cu2N4	94.0(2)
N1Cu1O4	179.3(2)	O5Cu2O1*w*	95.9(2)
N1Cu1N3	81.6(2)	N4Cu2O1*w*	94.5(2)
O2Cu2O1*w*	98.7(2)	N4Cu2O2	81.9(2)
O2Cu2O5	92.0(2)	N4Cu2O5	168.6(2

$[Cu_2(HL)(DMF)_2(H_2O)][Cu_2(HL)(SO_4)(H_2O)(DMF)_2]\cdot 2H_2O$ (4). A unit cell of **4** contains monocationic and monoanionic dinuclear complexes $[Cu_2(HL)(DMF)_2(H_2O)]^+$ (Figure 7a) and $[Cu_2(HL)(SO_4)(H_2O)(DMF)_2]^-$ (Figure 7b). Selected geometrical parameters are listed in Table 8. In both cation and anion the triply deprotonated ligand is bound to two copper(II) ions via ONN and ONO donor atoms. Square-pyramidal Cu2A and Cu2B atoms (τ_5 = 0.13 and 0.12, respectively) resided in ONO binding site of the ligand have the same coordination environment. Their fourth and fifth coordination sites are occupied by the DMF molecules. The fourth vertices in the bases around Cu1A (square-planar) and Cu1B (square-pyramidal, τ_5 = 0.09) are occupied by the water molecules. Cu1B is coordinated in its apical site by the O6B oxygen atom from SO_4^{2-} anion at 2.362(2) Å. Cu1A···Cu2A and Cu1B···Cu2B distances are at 4.7828(6) Å and 4.7957(6) Å, respectively. Cu1–N3–N4–Cu2 torsional angles are of 165.1(2)º and 165.7(2)° for complex cation and anion, respectively. The C−O distance in carbohydrazide fragment is practically the same in the complex cation (1.265(5) Å) and anion (1.267(5) Å). Also very similar are the C8−N2 bonds (1.363(5) Å for the cation and 1.350(5) Å for the anion), suggesting that O1 and O3 are the sites of deprotonation. The crystal structure packing motif can be characterised as 3D supramolecular architecture where the binuclear complexes as well as the solvate water molecules are linked through an extended system of hydrogen bonds N−H···O and O−H···O (Figure S9). Hydrogen bonding parameters are given in Table S1.

a)

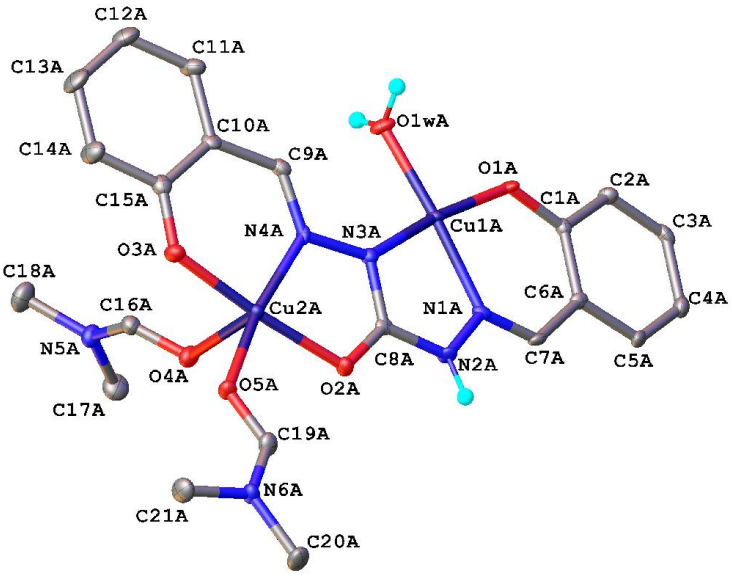

b)

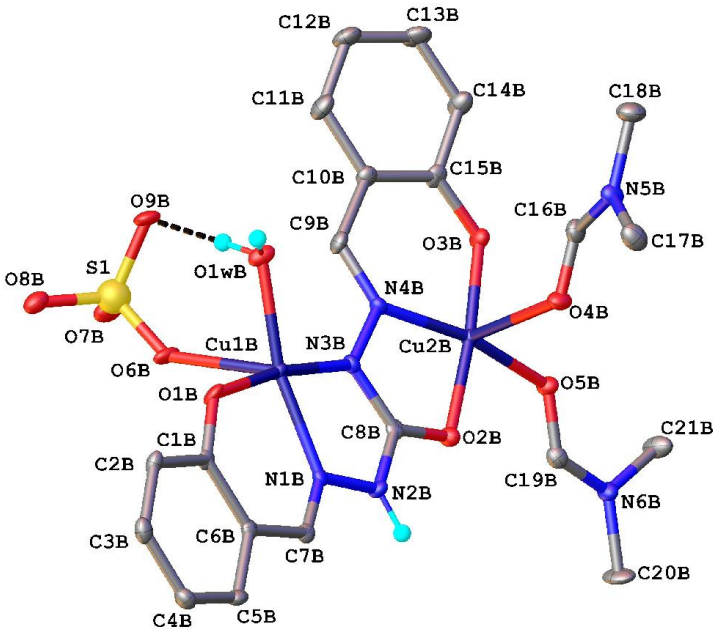

Figure 7. ORTEP view of the a) complex cation $[Cu_2(HL)(DMF)_2(H_2O)]^+$ and b) complex anion $[Cu_2(HL)(SO_4)(H_2O)(DMF)_2]^-$ in **4** with thermal ellipsoids drawn at 50% probability level.

Table 8. Selected bond distances (Å) and angles (°).

	A	B
Cu1–O1*w*	1.939(3)	2.008(3)
Cu1–O1	1.907(3)	1.923(3)
Cu1–O6		2.363(2)
Cu1–N1	1.945(3)	1.943(3)
Cu1–N3	1.987(3)	2.000(3)
Cu2–O2	1.962(3)	1.944(3)
Cu2–O3	1.897(3)	1.900(3)
Cu2–O4	2.374(3)	2.373(3)
Cu2–O5	1.979(3)	1.997(3)
Cu2–N4	1.937(3)	1.947(3)
N1–N2	1.386(4)	1.382(4)
N2–C8	1.363(5)	1.350(5)
C8–O2	1.265(5)	1.267(5)
C8–N3	1.337(5)	1.342(5)
N3–N4	1.395(4)	1.397(4)
C7–N1	1.278(5)	1.289(5)
C9–N4	1.293(5)	1.288(5)
O1*w*Cu1O6		80.3(1)
O1Cu1O1*w*	88.7(1)	91.4(1)
O1Cu1O6		89.7(1)
O1Cu1N1	91.9(1)	91.0(1)
O1Cu1N3	171.7(1)	171.3(1)
N1Cu1O1*w*	174.6(1)	165.7(1)
N1Cu1O6		113.8(1)
N1Cu1N3	81.0(1)	80.4(1)
N3Cu1O1*w*	98.8(1)	97.1(1)
N3Cu1O6		93.3(1)
O3Cu2O2	175.3(1)	174.9(1)
O3Cu2O5	91.0(1)	91.9(1)
O3Cu2O4	90.3(1)	91.6(1)
O3Cu2N4	94.6(1)	93.9(1)
O2Cu2O5	92.8(1)	91.9(1)
O2Cu2O4	91.9(1)	91.5(1)
O2Cu2N4	81.1(1)	81.8(1)
O5Cu2O4	98.6(1)	96.7(1)
N4Cu2O5	167.4(1)	168.1(1)
N4Cu2O4	92.7(1)	93.6(1)

$[Cu_4(HL)_2(HSO_4)(DMF)_2]HSO_4$ (5). The main structural unit in **5** represents a tetranuclear planar complex cation $[Cu_4(HL)_2(HSO_4)(DMF)_2]^+$ (Figure 8), which resembles the structure of **2**. Selected geometrical parameters are listed in Table 9. The Cu1 and Cu2 are separated at 4.8151(5) and 4.8149(5) Å with the torsion angle Cu1–N3–N4–Cu2 of 170.2(2) and

178.8(2), respectively for **A** and **B** ligands. Cu2A and Cu2B atoms adopt a square-pyramidal coordination geometry (τ_5 = 0.10 and 0.06, respectively) provided by the ONO donors of the Schiff base and an oxygen atom from adjacent ligand in the basal planes and an oxygen atom from the μ-HSO_4^- anion in the apical position. The bonds Cu2A–O1 of 2.304(2) Å and Cu2B–O2 of 2.340(2) Å are significantly longer than the rest of Cu–ligand bonds. The Cu1A and Cu1B atoms exhibit a square-planar coordination geometry provided by ONN donor atom sets from Schiff base ligand and an oxygen atom from DMF molecule. In addition, Cu1A and Cu1B atoms are coordinated, respectively in apical position by O1B at 2.742(2) Å and N3A at 2.930(2) Å atoms from another complex anion resulting in centrosymmetric octanuclear cationic species $[Cu_8(HL)_4(HSO_4)_2(DMF)_4]^{2+}$ (Figure 9) with Cu1A···Cu1B^i separation of 3.5494(5) Å. The above mentioned units are linked through O–H···O intermolecular H-bonds between coordinated HSO_4^- anions forming a polymeric chain across a centre of inversion, as shown in Figure S10. Further aggregation of the crystal structure occurs through hydrogen bonding with the participation of the HSO_4^- counterion, giving a 3D supramolecular architecture (Figure S11). The hydrogen bonding parameters are listed in Table S2.

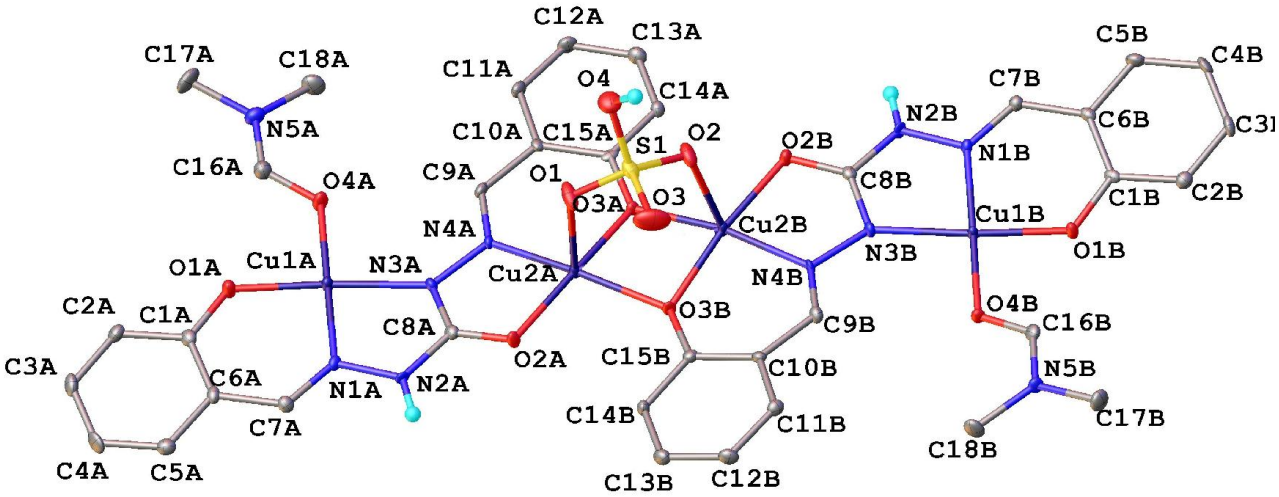

Figure 8. ORTEP view of $[Cu_4(HL)_2(HSO_4)(DMF)_2]HSO_4$ (**5**).

Table 9. Selected bond distances(Å) and angles (°).

	A	**B**
Cu1–O1	1.886(2)	1.8985(19)
Cu1–O4	1.976(2)	1.966(2)
Cu1–N1	1.936(2)	1.944(2)
Cu1–N3	2.008(2)	1.998(2)

Cu2A–O1	2.304(2)	
Cu2A–O3A	1.928(2)	
Cu2A–O3B	1.992(2)	
Cu2B–O2	2.340(2)	
Cu2B–O3B	1.942(2)	
Cu2B–O3A	1.982(2)	
Cu2–O2	1.929(2)	1.935(2)
Cu2–N4	1.945(2)	1.946(2)
N1–N2	1.383(3)	1.381(3)
N2–C8	1.358(4)	1.343(4)
C8–O2	1.275(3)	1.284(3)
C8–N3	1.331(4)	1.335(4)
N3–N4	1.406(3)	1.400(3)
C7–N1	1.293(4)	1.291(4)
C9–N4	1.277(4)	1.284(4)

O2Cu2N4	81.96(9)	81.65(9)
O3Cu2O2	171.61(8)	172.49(8)
O3Cu2N4	93.91(9)	93.11(9)
O2ACu2AO1	94.87(8)	
O2ACu2AO3B	102.32(8)	
O3ACu2AO1	92.93(8)	
O3ACu2AO3B	80.00(8)	
O3BCu2AO1	95.26(8)	
N4ACu2AO1	97.87(9)	
N4ACu2AO3B	165.81(9)	
O2BCu2BO2	90.85(8)	
Cu2BO3A	104.40(8)	
O3ACu2BO2	87.80(8)	
O3BCu2BO2	95.49(8)	
O3BCu2BO3A	79.91(8)	
N4BCu2BO2	101.56(9)	
N4BCu2BO3A	168.89(9)	

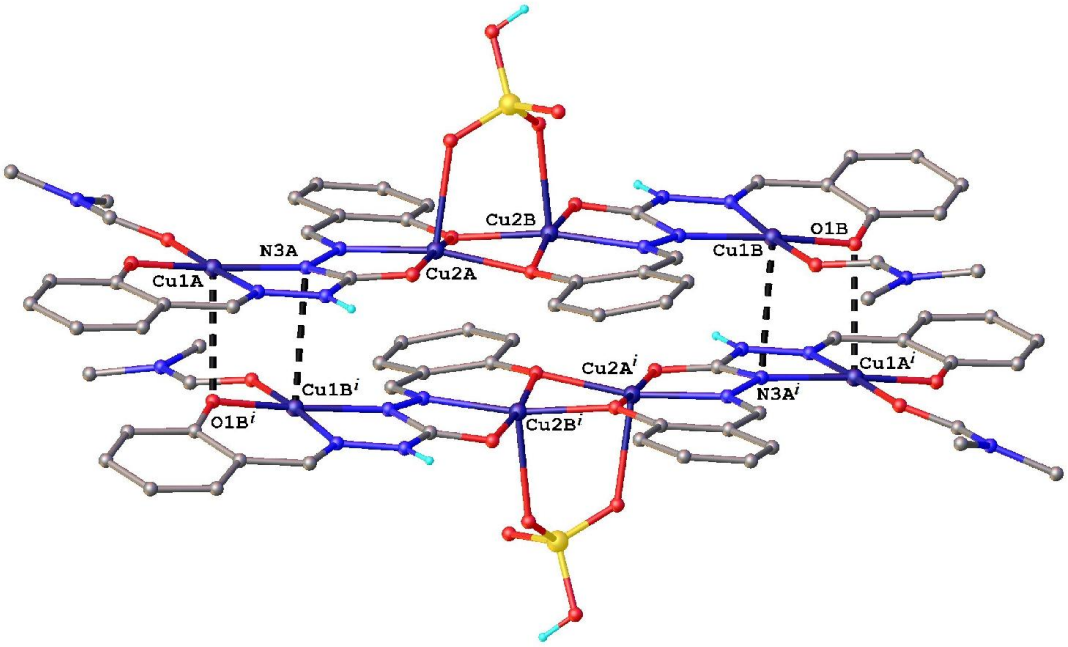

Figure 9. View of the octanuclear entity in **5**.

Magnetic properties. The magnetic properties of the compounds **1**–**3** have been investigated in the temperature range 2−300 K. For complex **1** at room temperature the $\chi_M T$-value amounts to 0.67 cm^3 K mol^{-1} (Figure 10). This value is slightly lower than the expected one of 0.75 cm^3 K mol^{-1} for two uncoupled spins with $S_1 = S_2 = {}^1/_2$. Cooling down to 30 K leads to a decrease of the $\chi_M T$-value to ≈ 0 cm^3 K mol^{-1}. Further cooling does not lead to any significant change of the $\chi_M T$-values. This indicates an antiferromagnetic interaction between the two copper centres. The magnetic data can be simulated satisfactorily by applying the isotropic exchange Hamilton operator $\hat{H} = -2J\,\hat{S}_1\hat{S}_2$. The best simulation was obtained with J = −77.34 cm^{-1} and $g_1 = g_2$ = 2.160, with the agreement factor $R = [\Sigma(\chi T_{obs} - \chi T_{calcd})^2/\Sigma(\chi T_{obs})^2] = 2.93 \times 10^{-2}$. A small TIP of 140×10^{-6} cm^3 K mol^{-1} was included while simulating the data.

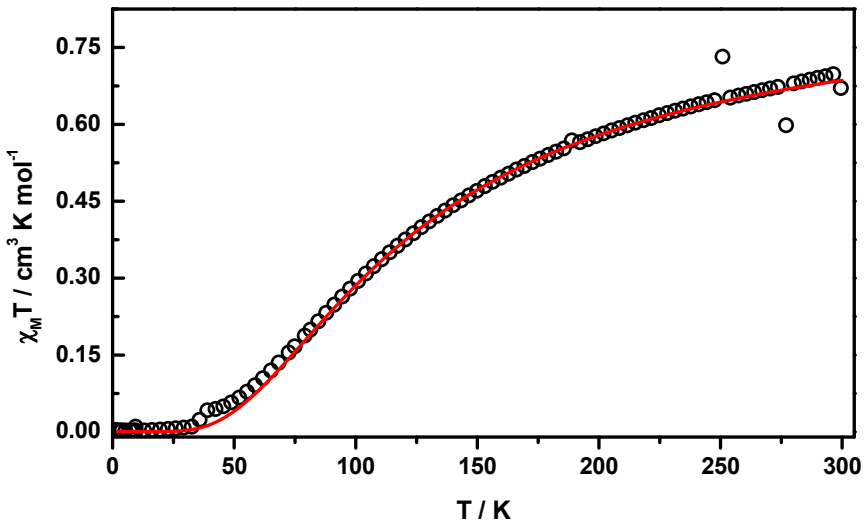

Figure 10. Plot of $\chi_M T$ vs T (○) for **1**. The solid red traces correspond to the best simulation with the values quoted in the text.

Complex **2** at room temperature shows a $\chi_M T$-value of 0.91 cm^3 K mol^{-1}, which is lower than the expected one of 1.50 cm^3 K mol^{-1} for four uncoupled spins with $S_1 = S_2 = S_3 = S_4 = {}^1/_2$ (Figure 11). By lowering the temperature the $\chi_M T$-value also decreases reaching a value of ≈ 0 cm^3 K mol^{-1} at 2 K. This indicates dominant antiferromagnetic interactions between the paramagnetic centres. The magnetic data can be simulated satisfactorily by applying the isotropic exchange Hamilton operator $\hat{H} = -2J_{ij}\Sigma\, \hat{S}_i\hat{S}_j$, with the model depicted in Figure S12. Two different coupling constants have to be taken into account, due to the different bridging mode between Cu1 and Cu2 (Cu3 and Cu4) and Cu2 and Cu2' (Cu3 and Cu3'). The two non-crystallographically symmetric tetrameric units were treated as equal, because of unsignificant differences in bond distances and angles. The couplings via O1/O6 to the next tetranuclear units to form chains were neglected, because of the expected small coupling constants by bridging via a non-magnetic orbital (d_z^2). The best simulation was obtained with $J_1 = -92.10$ cm^{-1}, $J_2 = -131.69$ cm^{-1} and $g_1 = g_2 = g_3 = g_4 = 2.00$, with the agreement factor $R = 3.59 \times 10^{-2}$. A paramagnetic impurity (10% with $S = ½$ and $\theta = -6.0$ K) has to be included to obtain a good simulation.

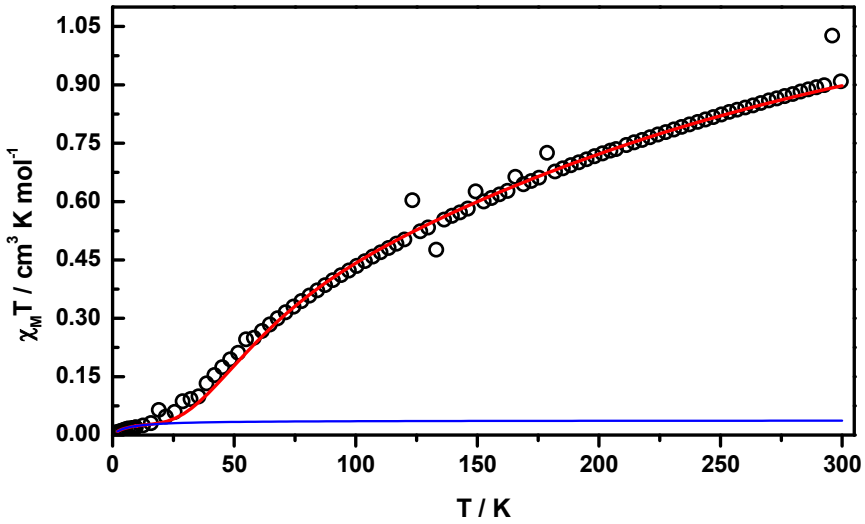

Figure 11. Plot of $\chi_M T$ vs T at 1 T as black circles for **2**. The solid red trace corresponds to the best simulation with the values described in the text, while the blue line indicates the presence of minor paramagnetic impurity.

Complex **3** at room temperature showed a $\chi_M T$-value of 0.63 cm^3 K mol^{-1}, which is slightly lower than the expected one of 0.75 cm^3 K mol^{-1} for two uncoupled spins with $S_1 = S_2 = {}^1/_2$ (Figure 12). Lowering the temperature leads to a decrease of the $\chi_M T$-value to ≈ 0 cm^3 K mol^{-1} at 40 K. Further cooling does not lead to a significant change of the $\chi_M T$-values. This indicates an antiferromagnetic interaction between the two copper centres. The magnetic data was simulated satisfactorily by applying the isotropic exchange Hamilton operator $\hat{H} = -2J\,\hat{S}_1\hat{S}_2$. The best simulation was obtained with $J = -78.14$ cm^{-1} and $g_1 = g_2 = 2.069$, with the agreement factor $R = 5.0 \times 10^{-3}$.

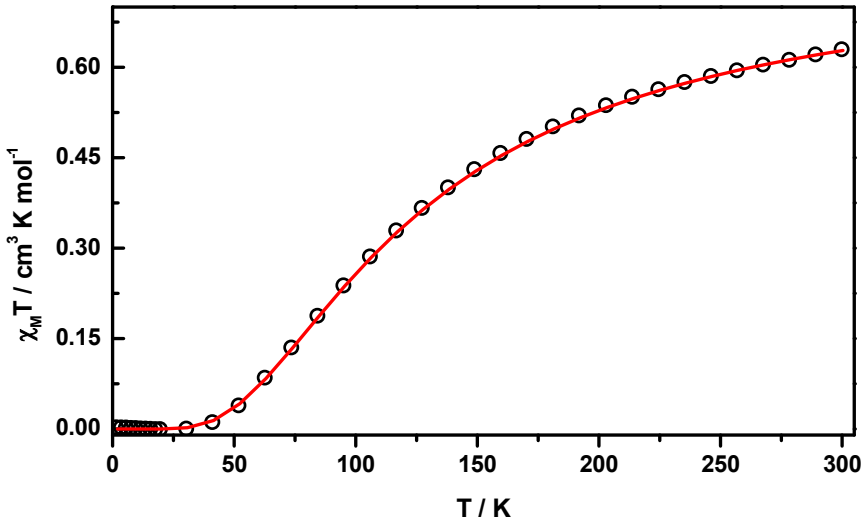

Figure 12. Plot of $\chi_M T$ vs T at 1 T as black circles for **3**. The solid red trace corresponds to the best simulation with the values described in the text.

Nearly identical antiferromagnetic interaction of –77.34 cm^{-1} and –78.14 cm^{-1} was observed for the copper ions connected via the N–N bridges in **1** and **3**. For **2** a slightly stronger antiferromagnetic interaction of –92.10 cm^{-1} was found, which is in good agreement with the values reported in the literature.[43,44,45] Strong antiferromagnetic interactions between the copper ions are determined by the twist angle of the two magnetic planes of the copper ions, which are nearly coplanar for the complexes studied. The differences in the strength of the antiferromagnetic interactions observed for **1**, **3** and **2** are based on the different coordination modes of the copper ions. In **1** and **3** one copper ion has a square-pyramidal or a square-planar coordination geometry respectively, while in **2** both copper ions are five-coordinate. In addition, the interaction via the two μ_2-phenolato bridges was taken into account for **2**. The estimated value of –131.69 cm^{-1} is in good agreement with the values reported in the literature.[46]

Electrochemistry. The cyclic voltammograms of **1** (in DMSO), **2** and **3** (in DMF) containing 0.2 M $TBAPF_6$ as a supporting electrolyte using a platinum wire working electrode are shown in Figure 13. The redox potentials are quoted against the decamethylferrocenium/decamethylferrocene couple ($DmFc^+$/DmFc). DmFc was added as an internal standard after voltammetric measurements of **1**–**3**. The electrochemical properties of

all three complexes are comparable. Upon reduction two distinct reduction peaks were observed in the cathodic region. The second reduction peak arises at more negative potentials and the separation between the first and the second reduction waves is around 50 mV for all three complexes. A marked cathodic shift in the redox potential from $E_{p/2}$ = –0.42 V to $E_{p/2}$ = –0.67 V vs $DmFc^+/DmFc$ couple occurs on passing from **3** to **2**. Even more negative first redox potential was observed for **1** with $E_{p/2}$ = –0.71 V vs $DmFc^+/DmFc$.

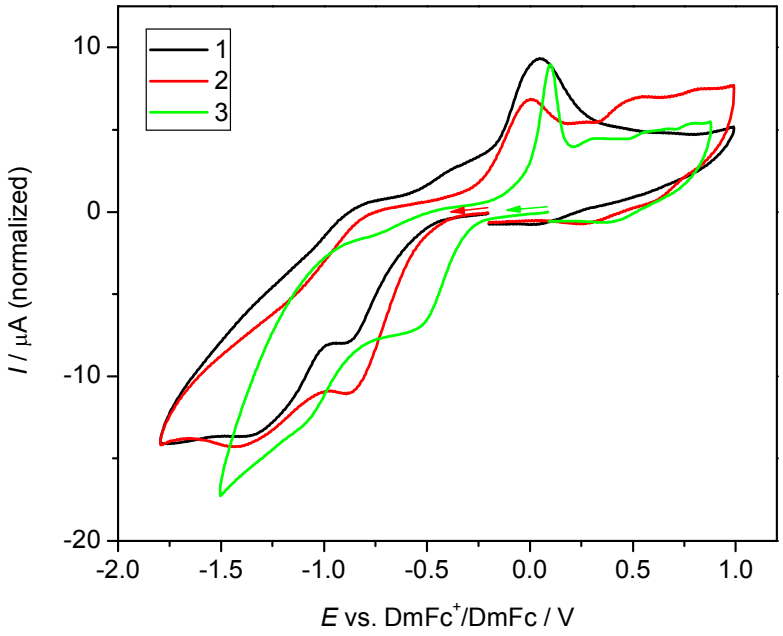

Figure 13. Comparison of cyclic voltammograms of **1** in DMSO (black trace), **2** (red trace) and **3** (green trace) in DMF measured at room temperature under argon (0.2 M $TBAPF_6$, scan rate 100 mV s^{-1}, platinum wire working electrode). Arrows indicate the starting potentials.

Dicopper(II) complexes show often two-step, one-electron reduction waves attributed to Cu(II)–Cu(II) + e → Cu(II)–Cu(I) and Cu(II)–Cu(I) + e → Cu(I)–Cu(I) redox processes, and the difference between the reduction potentials reflects the strength of the interaction between the copper(II) centers.[47,48] Controlled potential electrolysis performed at the first reduction peak for investigated samples **1**–**3** indicates the consumption of one electron per 2 : 1 copper to ligand species (n = 0.9). One electron reduction was also confirmed by comparison of the reduction wave height of equivalent amounts of decamethylferrocene (DmFc) and the investigated complexes (see Figure S13 for complex **3** as an example). DmFc oxidation is a one electron process and similar peak currents indicate the one electron reduction for **1**–**3** at

first cathodic peak (given similar diffusion coefficients). The corresponding metal-free ligand H_4L is reduced at more negative potentials when compared to the corresponding dicopper(II) complex (see red line in Figure S13). Therefore the first reduction wave for **1**−**3** can be attributed to Cu(II)–Cu(II) + e → Cu(II)–Cu(I) process. This was also clearly corroborated by ESR-spectroelectrochemistry. Complexes **1**−**3** in DMF at room temperature were EPR silent, confirming the presence of strong antiferromagnetic interaction between the paramagnetic copper(II) ions found from the temperature dependence of magnetic susceptibility. Upon reduction at the first cathodic peak an ESR signal due to paramagmetic Cu(II) nuclei arises (Figure S14), implying the formation of Cu(II)–Cu(I) species, where no antiferromagnetic interaction is expected.

It should be noted that cyclic voltammograms of **1**−**3** do not show anodic peaks upon scan in the cathodic direction indicating on irreversibility of the electrode processes. In the first cyclic voltammetry scan to the anodic potentials up to 1 V vs $DmFc^+$/DmFc no redox processes were observed (Figure S15a). However, upon going to the cathodic region up to the second reduction peak new redox processes are observable for **1**–**3** in the consecutive scans in the anodic region. The shape of voltammetric curve registered upon the second consecutive scan is different and anodic peaks of the products which are visible in the anodic part increase during consecutive scans (Figure S15b). This indicates irreversible step-by-step reduction of copper(II) ions in the dinuclear complexes upon cathodic scan followed by the formation of new species with a different redox behaviour.

Conclusion. Comparison of the experimentally determined and calculated by DFT methods pK_a values for H_4L and H_4L^S indicates that acid-base properties for the two ligands differ markedly. According to X-ray crystallography in complexes **1**–**5** the ligand acts as triply deprotonated base and adopts the *anti enol* configuration with two different metal-binding-sites. The counterion of the starting copper(II) salt and the solvent mixture used for the synthesis of complexes have a significant impact on both their composition and packing. The anions NO_3^-, SO_4^{2-} or HSO_4^- are involved in the complex formation in coordinated or non-bound to metal form. At the same time, compounds **1**, **3** and **4**, which contain respectively a noncoordinated NO_3^-, coordinated SO_4^{2-} and noncoordinated HSO_4^-, are dinuclear systems. In **2**, where NO_3^- acts both as coordinated and noncoordinated anion, tetranuclear units are formed. Complex **5**, in which the HSO_4^- plays a role of a bidentate bridging ligand, also

consists of tetranuclear units, that are further associated in octanuclear cationic assemblies $[Cu_8(HL)_4(HSO_4)_2(DMF)_4]^{2+}$. The packing of compounds studied is varied and depends on the possibilities for hydrogen-bonding and π-π* stacking interactions. In crystal structures of complexes **2**, **4** and **5** the packing can be characterised as a 3D supramolecular net, while in **1** and **3** as supramolecular aggregates of 1D and 2D types, respectively. Of note is also that **3**–**5** resulted from one pot synthesis. Temperature dependent magnetic susceptibility measurements indicate antiferromagnetic interaction between the paramagnetic Cu^{II} (d^9) centres in **1**–**3**. Consecutive irreversible one-electron reduction of both copper(II) centres is typical for **1**–**3** which have been investigated by cyclic voltammetry. Collectively the data obtained suggest that further deprotonation of the coordinated ligand $(HL)^{3-}$ in the presence of strong bases such as Et_3N or similar ones may be realised. Whether this will also lead to the formation of 24-membered octanuclear metallamacrocycles remains to be verified experimentally.

Acknowledgements. The financial support of the Science and Technology Assistance Agency (contract No. APVV-0202-10), Slovak Grant Agency VEGA (contract No. 1/0327/12) and the Hungarian Research Foundation OTKA PD103905 are gratefully acknowledged. This work was also supported by the Slovak-Austrian and Austrian-Romanian bilateral mobility grants SK–02/2013–2014 and RO–01/2014–2015 and by a grant of the Ministry of National Education, CNCS – UEFISCDI, project number PN-II-ID-PCE-2012-4-0261. The calculations were performed in the Computing Centre of the Slovak Academy of Sciences using the supercomputing infrastructure acquired in project ITMS 26230120002 and 26210120002 (Slovak infrastructure for high-performance computing) supported by the Research & Development Operational Programme funded by the ERDF. We thank Alexander Roller for collection of X-ray data sets.

Note

Dedicated to Prof. Dr. Vukadin M. Leovac on the occasion of his 70th birthday.

Appendix A. Supplementary data

CCDC 978466, 978467, 978468, 978469 and 978470 contain the supplementary crystallographic data for complexes **1**–**5**. The data can be obtained free of charge via

http://www.ccdc.cam.ac.uk/conts/retrieving.html, or from the Cambridge Crystallographic Data Centre, 12 Union Road, Cambridge CB2 1EZ, UK; fax: (+44) 1223-336-033; or e-mail: deposit@ccdc.cam.ac.uk. The data also include X-ray diffraction structure of H_4L and H_4L^S (Figure S1), experimental pK_a values of selected compounds in aqueous solution and in DMSO (Table S1), UV−vis absorption spectra of the ligand H_4L^S recorded at different pH values (Figure S2), the dependence of experimental pK_a values measured in DMSO on pK_a values for aqueous solutions (Figure S3), hydrogen bonding parameters for **1–5** (Table S2), one-dimensional supramolecular architecture in **1** (Figure S4), **t**wo stepped polymeric chains in the crystal structure of **2** (Figure S5), a fragment of 3D supramolecular network in the crystal of **2** (Figure S6), hydrogen bonded dimeric units in **3** (Figure S7), view of 2D supramolecular layer in the crystal structure of **3** (Figure S8), a fragment of 3D supramolecular network in the crystal of **4** (Figure S9), one dimensional polymeric chain in the crystal structure of **5** (Figure 10), a fragment of 3D supramolecular network in the crystal of **5** (Figure S11), coupling scheme for **2** (Figure S12), cyclic voltammogram of **3** in 0.2 M $TBAPF_6$/DMF in the presence of DmFc (Figure S13), oxidation of **2** in 0.2 M $TBAPF_6$/DMF (Figure S14) and cyclic voltammograms of **2** in 0.2 M $TBAPF_6$/DMF upon redox cycling (2 consecutive scans) (Figure S15).

Supplementary data associated with this article can be found, in the online version, at doi:10.1016/j.poly.2013.

References

1. L. Zhao, V. Niel, L. K. Thompson, Z. Xu, V. A. Milway, R. G. Harvey, D. O. Miller, C. Wilson, M. Leech, J. A. K. Howard, S. L. Heath, Dalton Trans. (2004) 1446−1455.

2. T. L. Kelly, V. A. Milway, H. Grove, V. Niel, T. S. M. Abedin, L. K. Thompson, L. Zhao, R. G. Harvey, D. O. Miller, M. Leech, A. E. Goeta, J. A. K. Howard, Polyhedron 24 (2005) 807−821.

3. S. Sen, C. R. Choudhury, P. Talukder, S. Mitra, M. Westerhausen, A. N. Kneifel, C. Desplanches, N. Daro, J.-P. Sutter, Polyhedron 25 (2006) 1271−1278.

4. J. D. Ranford, J. J. Vittal, Yu. M. Wang, Inorg. Chem. 37 (1998) 1226−1231.

5. K. V. Shuvaev, L. N. Dawe, L. K. Thompson, Dalton Trans. 39 (2010) 4768–4776.

6. D.-Y. Wu, O. Sato, Y. Einaga, C.-Y. Duan, Angew. Chem. Int. Ed. 48 (2009) 1475–1478.
7. E. Manoj, M.R. Prathapachandra Kurup, H.-K. Fun, Inorg. Chem. Commun. 10 (2007) 324−328.
8. M. Moustapha Sow, O. Diouf, M. Gaye, A. Salam-Sall, G. Castro, A. Pérez-Lourido, L. Valencia, A. Ganeschi, L. Sorace, Cryst. Growth. Des. 13 (2013) 4172−4176.
9. E. Manoj, M. R. Prathapachandra Kurup, H.-K. Fun, A. Punnoose, Polyhedron 26 (2007) 4451−4462.
10. A. Bacchi, A. Bonini, M. Carcelli, F. Ferraro, E. Leporati, C. Pelizzi, G. Pelizzi, J. Chem. Soc., Dalton Trans. (1996) 2699−2705.
11. V. Lozan, P.-G. Lassahn, C. Zhang, B. Wu, C. Janiak, G. Rheinwald, G. H. Lang. Z. Naturforsch. 58b (2003) 1152−1164.
12. M. U. Anwar, L. K. Thompson, L. N. Dawe, F. Habib, M. Murugesu, Chem. Commun. 48 (2012) 4576–4578.
13. N. M. Randell, M. U. Anwar, M. W. Drover, L. N. Dawe, L. K. Thompson, Inorg. Chem. 52 (2013) 6731–6742.
14. G. R. Bustos, O. Burdkhardt, R. Schrebler, D. Carrilo, Inorg. Chem. 29 (1990) 3996−4002.
15. J. Dan, S. Seth, S. Chakraborty, Acta Cryst. C43 (1987) 1114−1116.
16. (a) R. Bikas, P. M. Anarjan, S. W. Ng, E. R. T. Tiekink, Acta Cryst. E68 (2012) o193; (b) B. Schmitt, T. Gerber, E. Hosten, R. Betz, Acta Cryst. E67 (2011) o2206-o2207.
17. L. Du, W. Zhang, Acta Cryst. E66 (2010) o2645.
18. Q.-P. He, B. Tan, Z.-H. Lu, Acta Cryst. E66 (2010) o2968.
19. C. Bustos, O. Burckhardt, R. Schrebler, D.Carrillo, A. M. Arif, A. H. Cowley, C. M. Nunn, Inorg. Chem. 29 (1990) 3996-4001.
20. M. A. Affan, Y. Z. Liew, F. Ahmad, M. Shamsuddin, B. M. Yamin, Ind. J. Chem. 46A (2007) 1063−1068.
21. (a) V. A. Kogan, V. V. Lukov, V. M. Novotortsev, I. L. Eremenko, G. G. Aleksandrov, Russ. Chem. Bull. 43 (2005) 600−605; (b) L. D. Popov, Yu. P. Topolova, V. V. Lukov, I. N. Shcherbakov, V. A. Kogan, A. V. Mishchenko, Russ. J. Gen. Chem. 78 (2008) 2094–2099.
22. D. Dragancea, V.B. Arion, S. Shova, E. Rentschler, N.V. Gerbeleu. Angew. Chem. Int. Ed. 44 (2005) 7938-7942.
23. R. Yanping, D. Rongbin, W. Liufang, W. Jigui, Synth. Commun. 29 (1999) 613−617.
24. H. M. Irving, M. G. Miles, L. D. Pettit, Anal. Chim. Acta 38 (1967) 475–488.

25. SCQuery, The IUPAC Stability Constants Database, Academic Software (Version 5.5), Royal Society of Chemistry, 1993−2005.

26. L. Zékány, I. Nagypál, in: D.L. Leggett (Ed.), Computational Methods for the Determination of Stability Constants, Plenum Press, New York, 1985, pp. 291–353.

27. V. Barone, M. Cossi, J. Phys. Chem. A102 (1998) 1995–2001.

28. M. Cossi, N. Rega, G. Scalmani, V. Barone, J. Comp. Chem. 24 (2003) 669−681.

29. M.J. Frisch, G.W. Trucks, H.B. Schlegel, G.E. Scuseria, M.A. Robb, J.R. Cheeseman, J.A. Montgomery Jr., T. Vreven, K.N. Kudin, J.C. Burant, J.M. Millam, S.S. Iyengar, J. Tomasi, V. Barone, B. Mennucci, M. Cossi, G. Scalmani, N. Rega, G.A. Petersson, H. Nakatsuji, M. Hada, M. Ehara, K. Toyota, R. Fukuda, J. Hasegawa, M. Ishida, T. Nakajima, Y. Honda, O. Kitao, H. Nakai, M. Klene, X. Li, J.E. Knox, H.P. Hratchian, J.B. Cross, C. Adamo, J. Jaramillo, R. Gomperts, R.E. Stratmann, O. Yazyev, A.J. Austin, R. Cammi, C. Pomelli, J.W. Ochterski, P.Y. Ayala, K. Morokuma, G.A. Voth, P. Salvador, J.J. Dannenberg, V.G. Zakrzewski, S. Dapprich, A.D. Daniels, M.C. Strain, O. Farkas, D.K. Malick, A.D. Rabuck, K. Raghavachari, J.B. Foresman, J.V. Ortiz, Q. Cui, A.G. Baboul, S. Clifford, J. Cioslowski, B.B. Stefanov, G. Liu, A. Liashenko, P. Piskorz, I. Komaromi, R.L. Martin, D.J. Fox, T. Keith, M.A. Al-Laham, C.Y. Peng, A. Nanayakkara, M. Challacombe, P.M.W. Gill, B. Johnson, W. Chen, M.W. Wong, C. Gonzalez, J.A. Pople, Gaussian 03, Revision A.1, Gaussian, Inc., Pittsburgh PA, 2003.

30. J. T. Muckerman, J. H. Skone, M. Ning, Y. Wasada-Tsutsui, Biochim. Biophys. Acta 1827 (2013) 882–891 and the references cited therein.

31. G.A.A. Saracino, R. Improta, V. Barone, Chem. Phys. Let. 373 (2003) 411−415 and the references cited therein.

32. M. Sramko, M. Smiesko, M. Remko, J. Biomolec. Struct. Dynam. 25 (2008) 599−607 and the references cited therein.

33. I. Alkorta, J. Elguero, R. Gallo, Cent. Eur. J. Chem. 11 (2013) 1711−1722 and the references cited therein.

34. *SAINT-Plus*, v. 7.06a, Bruker-Nonius AXS Inc., Madison, WI, **2004**; *APEX2*, Bruker-Nonius AXS Inc., Madison, WI, **2004**.

35. G. M. Sheldrick, *Acta Crystallogr. Sect. A* 64 (2008) 112.

36. E. Bill, Max-Planck Institute for Bioinorganic chemistry, Mülheim, http://ewww.mpi-muelheim.mpg.de/bac/logins/bill/julX_en.php".

37. É. A. Enyedy, G. M. Bognár, N. V. Nagy, T. Jakusch, T. Kiss, D. Gambino, Polyhedron 67 (2014) 242–252.

38. É. A. Enyedy, É. Zsigó, N. V. Nagy, C. R. Kowol, A. Roller, B. K. Keppler, T. Kiss, Eur. J. Inorg. Chem. (2012) 4036–4047.

39. M. Born, Z. Phys. 1 (1920) 45–48.

40. Covington, A. K., Dickinson, T. (Eds): Physical chemistry of organic solvent systems. Plenum Press, London, 1973.

41. Y. Fu, L. Liu, R.-Q. Li, R. Liu, Q.-X. Guo*, J. Am. Chem. Soc.* 126 (2004) 814–822. (2004).

42. A. W. Addison, T. N. Rao, J. Reedijk, J. van Rijn, G. C. Verschoor, J. Chem. Soc. Dalton Trans. (1984) 1349–1356.

43. Z. Xu , L. K. Thompson, D. O. Miller, Inorg. Chem. 36 (1997) 3985–3995.

44. L. K. Thompson, Z. Xu, A. E. Goeta, J. A. K. Howard, H. J. Clase, D. O. Miller, Inorg. Chem. 37 (1998) 3217–3229.

45. K. V. Shuvaev, T. S. M. Abedin, C.A. McClary, L. N. Dawe, J. L. Collins, L. K. Thompson, Dalton Trans. (2009) 2926–2939.

46. O. Chiari, T. Piovesana, P. F. Zanazzi, Inorg. Chem. 26 (1987) 952–955.

[47] P. Kamatchi, S. Selvaraj, M. Kandaswamy, Polyhedron 24 (2005) 900–908.

[48] A. Jana, S. Mohanta, Inorg. Chim. Acta 405 (2013) 265–273 and the references cited therein.

Graphical Abstract

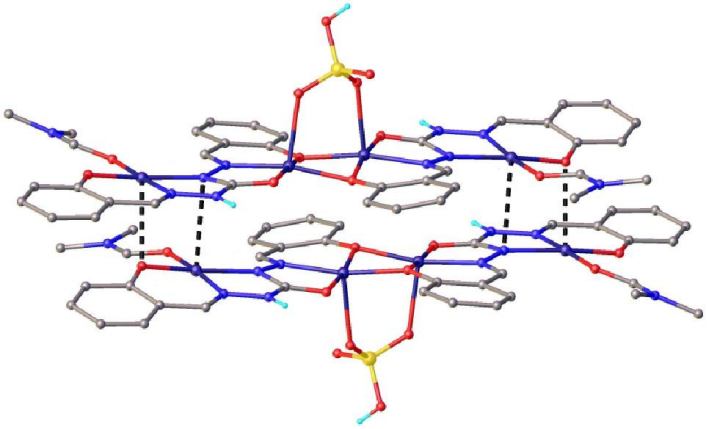

The acid-base properties of 1,5-bis(2-hydroxybenzaldehyde)carbohydrazone and its thioanalogue have been studied experimentally and by DFT methods. Five copper(II) complexes with 1,5-bis(2-hydroxybenzaldehyde)carbohydrazone have been synthesised and characterised by X-ray crystallography. The ditopic ligand possesses two binding sites able to accommodate transition metal ions. Magnetic measurements showed antiferromagnetic interactions between copper(II) centres.